

Anomalous size effects with fixed criticality in bistable flexible mechanical metamaterials

Zehuan Tang^{a,b}, Tingfeng Ma^{a,*}, Boyue Su^a, Qing Xia^c, Pengfei Kang^a, Bowei Wu^a

^a Zhejiang-Italy Joint Lab for Smart Materials and Advanced Structures, School of Mechanical Engineering and Mechanics, Ningbo University, Ningbo 315211, China

^b Key Laboratory of Mechanics on Environment and Disaster in Western China, The Ministry of Education of China, Lanzhou University, Lanzhou 730000, China

^c School of Civil Engineering and Transportation, South China University of Technology, Guangzhou, 510641, Guangdong, China

ABSTRACT

When the structure deformation is dominated by the low-energy deformation mode, the structure hardens with the increase in the size (number of units) at small sizes. This anomalous behavior will eventually disappear with the decay length of the finite structure converging to a size-independent characteristic quantity, but the specific critical point at which the anomalous behavior disappears still cannot be accurately and concisely described. Here, under two steady states of the bistable chain, we observe anomalous size effects with constant and oscillating criticality (the proportion of inhomogeneous deformation), two criticalities exactly separate the increasing and decreasing intervals of stiffness variation. They are interrelated because of the implied symmetries between the two steady states, on the other hand, they are distinguished because of the opposite superposition mode under the two steady states. Specifically, the constant criticality corresponds to the anomalous size effect achieved by the competition mechanism, while the oscillating criticality reveals an anomalous size effect achieved by the new mechanism (cancellation mechanism). In the anomalous size effect achieved by the cancellation mechanism, the singular characteristics generated by the completely cancelled deformation make it very robust. This robustness reflects in that the anomalous effects are no longer limited to linear small deformation, but it can still be observed stably in nonlinear large deformation. Our study reinterprets the anomalous size effect at a quantitative level, and the proposed cancellation mechanism expands the possible application range of this anomalous effect.

Keywords: Size effect; Low-energy deformation; Criticality; Nonlinearity; Robustness

1. Introduction

Flexible mechanical metamaterials (FlexMMs) usually refer to metamaterials composed of flexible hinges and stiffer elements (Deng et al., 2021), and current studies of such metamaterials have focused on porous structures, origami structures, and bistable plates. Taking the widely studied porous structure as an example, it has attracted attention because of its negative Poisson ratio under uniaxial compression (Bertoldi et al., 2010). Subsequently, extensive research has been carried out in porous structures, as well as in structures derived from them, such as adjustable Poisson ratios (Dudek et al., 2023, Khan et al., 2021), vector solitons (Deng et al., 2017, Li et al., 2021, Zhang et al., 2023), and recently shock-absorbing metamaterials that combine stiffness and dissipation (Liu et al., 2024).

In a series of studies on FlexMMs, flexible hinges are often modeled as a combination of multiple springs (Demiquel et al., 2024, Liang & Crosby, 2020, Jiao et al., 2024), where the parameters of the torsion spring are likely to have the greatest impact on the response (Meeussen et al., 2024, Mizzi & Spaggiari, 2020). When the torsional stiffness is zero (Zhou et al., 2021) or small enough to be negligible (Ma et al., 2018), the structure with geometric asymmetry will acquire non-trivial topological features, and then realize topologically protected zero-energy modes (Kane & Lubensky, 2014, Coulais et al., 2017) or solitons (Chen et al., 2014, Ma et al., 2023). However, except for purely mechanism materials connected by ideal hinges, it is difficult for the typical FlexMMs to meet the condition that the torsional stiffness is strictly zero (Meeussen et al., 2024). When the torsional stiffness is not negligible (Demiquel et al., 2023, Li et al., 2022, Vahabi et al., 2016), usually in the static state, the structure can only support the low-energy deformation mode, which is a non-propagating mode (Tang et al., 2024). Compared with the topological zero-energy mode, the low-energy deformation mode does not have the feature of localization on the specific side, but the property of decay only from the excitation point also makes

it have a series of interesting mechanical behaviors. For example, low-energy deformation on both sides can form a domain wall that separates two phases, and the configuration of the domain wall can be regulated by placing defects at different locations (Deng et al., 2020). At the same time, the decay property also makes the low-energy deformation conformal, and its distribution is affected by the load distribution at the boundary (Czajkowski et al., 2022). Furthermore, nonlinearity also gives more possibilities for the distribution of low-energy deformation (Medina et al., 2023, Zhang et al., 2019).

Overall, due to low-energy deformation sensitive to defects or constraints (Florijn et al., 2014), boundary conditions (Zheng et al., 2022, Liang & Crosby, 2020) and nonlinearity (Deng et al., 2020), current researches on low-energy deformation mostly focus on achieving specific deformation distributions by using these properties, and then achieving different effective stiffness through different deformation distributions (Deng et al., 2020, Li et al., 2024). However, since the unit cells of mechanical metamaterials cannot be considered as vanishingly small like in ordinary crystals, the size of the structure is no longer a factor that can be ignored. For example in small-size structures, the ordinary Cauchy continuum mechanics theory is no longer applicable (Kadic et al., 2018), and the effective properties (such as effective stiffness) of a small-size structure may be significantly different from those of a large size (Ziemke et al., 2019). In the monostable chain bearing low-energy deformation, the relationship between the stiffness and the structure size is further revealed (Coulais et al., 2018), the anomalous phenomenon that the structure stiffness increases with the size increase was captured by the discrete model, and an size-independent characteristic length scale (Frenzel et al., 2017) was defined in the continuum model to estimate the range of this anomalous phenomenon. Here, we also observe the anomalous size effect (the stiffness increases first and then decreases with the increase in size) in the bistable chain, in particular, under any initial configuration and any parametric flexural hinge, this behavior of stiffness increasing with size in the bistable chain has a fixed constant criticality or oscillating criticality. In further analysis, we found that the oscillating criticality actually corresponds to the compliance of the

structure tending to zero, this unique property not only intuitively proves that the constant in the constant criticality can only take 0.5, but more importantly, it reveals a new mechanism (cancellation mechanism) to achieve the anomalous size effect. The anomalous size effect achieved by the cancellation mechanism has an extremely large maximum stiffness value, which makes it robust in nonlinear large deformation.

2. Bistable flexible mechanical metamaterials

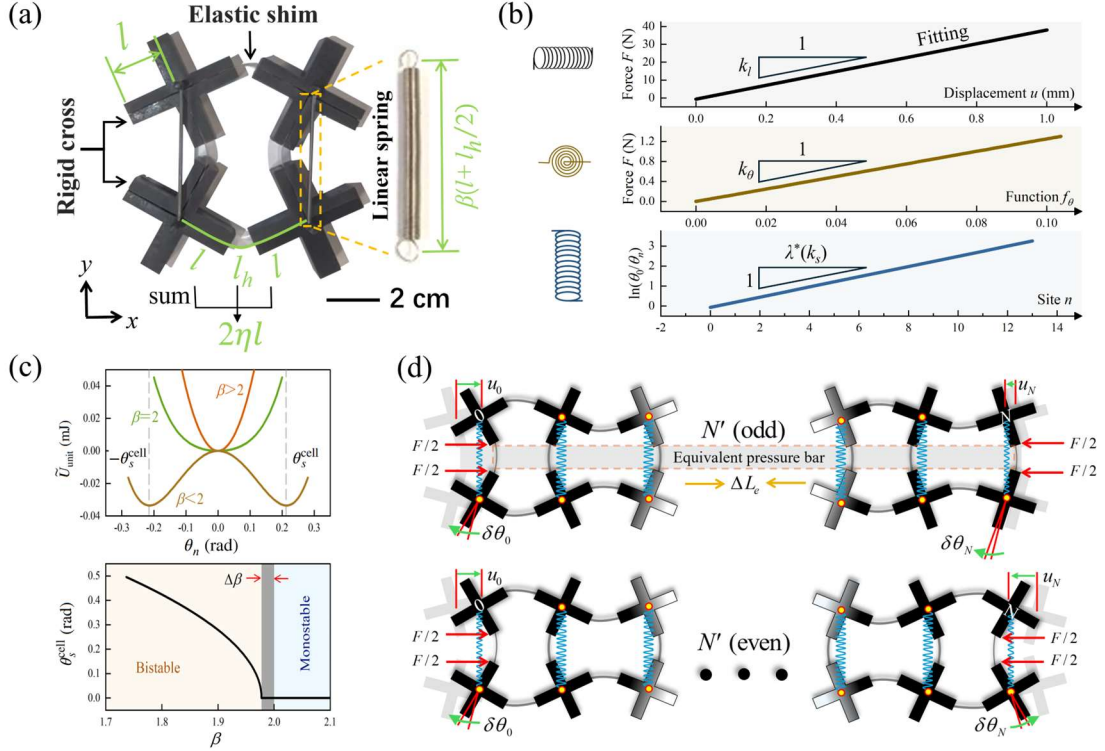


Fig. (1). (a) Bistable unit. (b) Three equivalent stiffness of shims, the experimental scheme refers to article (Tang et al., 2024). (c) The figure above shows the elastic energy of a bistable unit \tilde{U}_{unit} , where $\tilde{U}_{\text{unit}} = 8k_\theta\theta_n^2 + k_t(\eta l)^2\{(2\cos\theta_n - \beta)^2 - (2 - \beta)^2\}$. The figure below shows the change of equilibrium angle with β . (d) Modeling schematic diagram of the odd-node chain and even-node chain.

The bistable units are shown in Fig. 1(a), which is assembled from rigid crosses with elastic shims. The arm length of the rigid cross is l , and the length and thickness of the shim are $l_h = 8$ mm and $l_t = 0.2$ mm, respectively. Fig. 1(a) also shows that after the cross and shim are assembled, the actual length of the moment arm of the cross is ηl , where $\eta = 1 + l_h / (2l)$. The bistable property of units is realized by a pre-stretched linear spring connected between the center of the upper and lower cross

([Movie S1](#)). The stiffness of the linear spring between the centers is $k_l = 0.15$ N/mm, and its original length is l_{h0} , where l_{h0} is expressed by β as $l_{h0} = \beta(l + l_h/2)$. The shim is equivalent to a combination of stretching, torsional, and shearing linear springs, as shown in Fig. 1(b), and the equivalent stiffness of the three springs is $k_l = 35.14$ N/mm, $k_\theta = 3.17$ N • mm², $k_s = 0.71$ N/mm. We choose springs with different original lengths (namely different β) to achieve different equilibrium angles and the number of steady states. When $\beta \geq 2$ (the spring is pre-compressed), the unit has only one steady state $\theta_n = 0$. When $\beta < 2$ (the spring is pre-stretched), the unit has two symmetrical steady states $\theta_n = \theta_s^{\text{cell}}$ and $\theta_n = -\theta_s^{\text{cell}}$ ($\theta_s^{\text{cell}} > 0$), where the change of θ_s^{cell} with β is shown in Fig. 1(c). The gray area with a width $\Delta\beta$ in Fig. 1(c) is the ineffective adjustment area of β , which appears because the moment arm ($\eta l \sin \theta_n$) of the pre-stretched force and the torque of the shim ($k_\theta \theta_n$) are same order infinitesimal, and the pre-stretched force is not enough to make the cross rotate.

The bistable units are connected into a chain with N' ($N' = N + 1$) nodes, as shown in Fig. 1(d). In order to ensure that each node has an equal equilibrium angle under the initial state, at both ends of the chain, the thickness of the shim connecting the upper and lower crosses is chosen to be $l_t / 2$ (the torsional stiffness of the shim with thickness $l_t / 2$ is equivalent to $k_\theta / 2$, in addition, changes in k_l and k_s of the shim at this position do not affect the response of the chain), while the stiffness of the linear spring between the centers is selected as $k_l / 2$, as shown by the light gray shim and light blue spring at both ends in Fig. 1(d). In [Movie S2](#), the above design scheme is proved to be feasible by experiments and simulations. The equilibrium angles $\bar{\theta}$ of each node satisfy:

$$6k_\theta \bar{\theta} = k_l (\eta l)^2 (2 \cos \bar{\theta} - \beta) \sin \bar{\theta}. \quad (1)$$

According to Eq. (1), the chain of $\beta < 2$ has two kinds of initial configuration, which are denoted as $\bar{\theta} = \theta_s$ and $\bar{\theta} = -\theta_s$.

A pair of forces F are applied to both ends of the chain, as shown in Fig. 1(d), the equilibrium equations for the translation are established as follows ([the derivation is detailed in Appendix A](#)):

$$-F / 2 = k_l [(u_1 - u_0) + \eta l (\delta\theta_1 + \delta\theta_0) \sin \bar{\theta}], \quad (2a)$$

$$0 = k_l [u_{n+1} + u_{n-1} - 2u_n + \eta l (\delta\theta_{n+1} - \delta\theta_{n-1}) \sin \bar{\theta}], n \in [1, N - 1] \quad (2b)$$

$$F / 2 = -k_l [(u_N - u_{N-1}) + \eta l (\delta\theta_{N-1} + \delta\theta_N) \sin \bar{\theta}]. \quad (2c)$$

The equilibrium equations for the rotation are as follows:

$$Fl(\eta \sin \bar{\theta} + \cos \bar{\theta}) / 2 = k_\theta(\delta\theta_1 + 2\delta\theta_0) - k_s l^2(\delta\theta_1 - \delta\theta_0)\cos^2 \bar{\theta} - (k_t / 2)(\eta l)^2 [2 \cos(2\bar{\theta}) - \beta \cos \bar{\theta}] \delta\theta_0, \quad (3a)$$

$$F\eta l \sin \bar{\theta} = k_\theta(\delta\theta_{n+1} + \delta\theta_{n-1} + 4\delta\theta_n) - k_s l^2(\delta\theta_{n+1} + \delta\theta_{n-1} - 2\delta\theta_n)\cos^2 \bar{\theta} - k_t(\eta l)^2 [2 \cos(2\bar{\theta}) - \beta \cos \bar{\theta}] \delta\theta_n, n \in [1, N-1] \quad (3b)$$

$$Fl(\eta \sin \bar{\theta} \pm \cos \bar{\theta}) / 2 = k_\theta(\delta\theta_{N-1} + 2\delta\theta_N) - k_s l^2(\delta\theta_{N-1} - \delta\theta_N)\cos^2 \bar{\theta} - (k_t / 2)(\eta l)^2 [2 \cos(2\bar{\theta}) - \beta \cos \bar{\theta}] \delta\theta_N. \quad (3c)$$

3. Size effects under the two steady states

3.1. Numerical and experimental results

Eqs. (2) and (3) are rewritten in the matrix form:

$$[F] = [K][U]. \quad (4)$$

The one-dimensional chain in Fig. 1(d) is regarded as a pressure bar, and the length of the pressure bar is the distance between the acting points of forces at both ends. After loading force F , the change in bar length is denoted as ΔL_e , and the effective stiffness of the one-dimensional chain can be written as

$$k_e = \frac{F}{\Delta L_e} = \frac{F}{u_0 - u_N + l(\delta\theta_0 \pm \delta\theta_N) \cos \bar{\theta}}. \quad (5)$$

Substituting the numerical solution of Eq. (4) into Eq. (5) yields the results of the discrete model.

For the odd-node chain, Fig. 2(b) shows the variation of its effective stiffness with size. Experimental and numerical results show that the effective stiffnesses under the two initial configurations are completely coincident, and they both decrease with the increase in size. This coincidence behavior is essentially due to the mirror symmetry between the two steady states of the odd-node chain, the schematic diagram of the mirror symmetry is shown in Fig. 2(a). The mirror symmetry makes the deformation distributions under $\bar{\theta} = \theta_s$ (denoted u_n^+ and $\delta\theta_n^+$) and the deformation distributions under $\bar{\theta} = -\theta_s$ (denoted u_n^- and $\delta\theta_n^-$) satisfy the relationship $u_{N-n}^+ = -u_n^-$ and $\delta\theta_{N-n}^+ = -\delta\theta_n^-$, and the above relation can also be obtained by the transformation $\bar{\theta} \rightarrow -\bar{\theta}$ in Eqs. (2) and (3). Fig. 2(c) shows this deformational symmetry between two steady states by using the angular deformation distribution as an example. In a word, the mirror symmetry of the odd-node chain ensures that the

stiffnesses under the two initial configurations are equal.

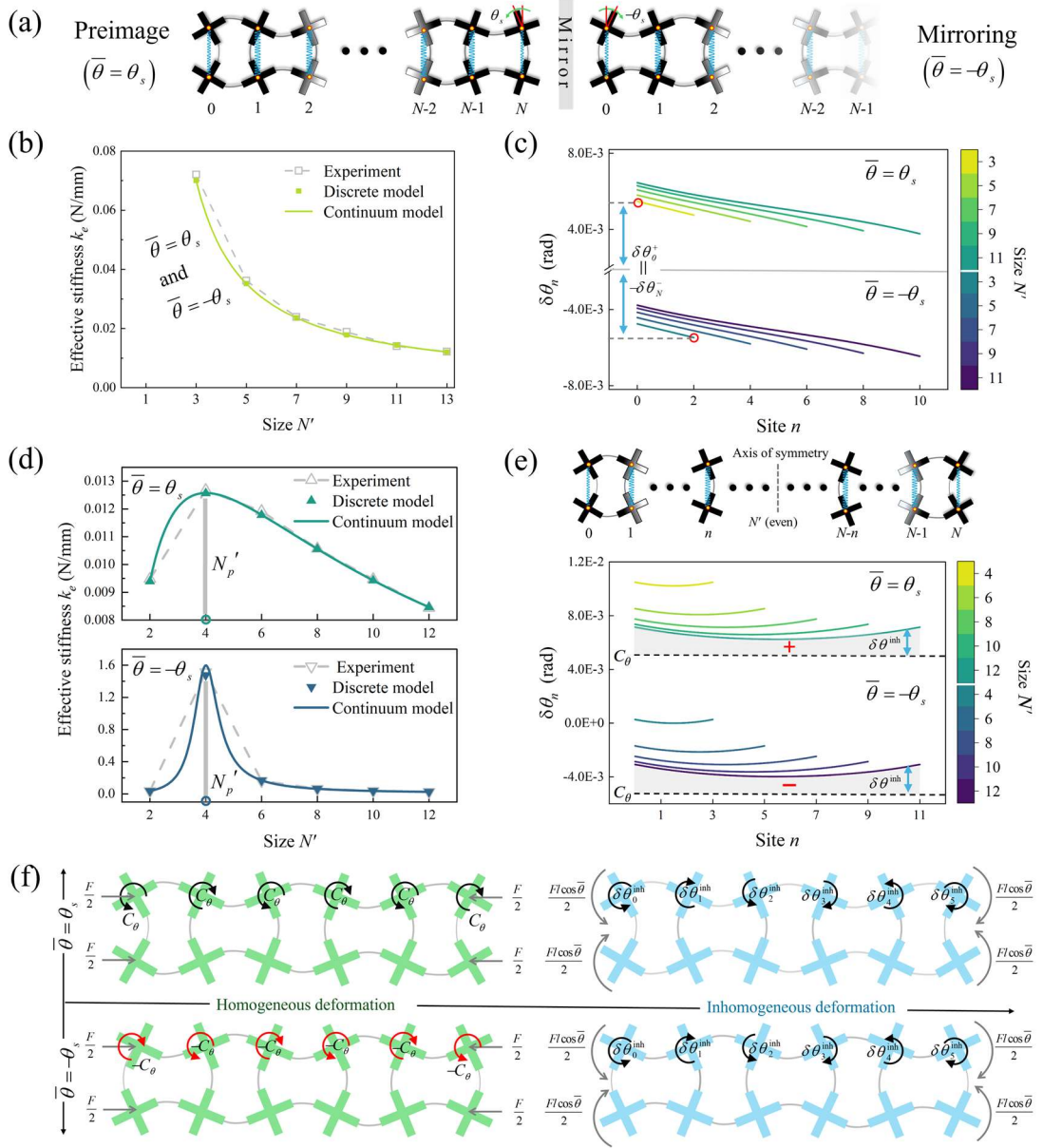


Fig. 2. (a) The odd-node chain has mirror symmetry between the two steady states. (b) In the odd-node chain, the effective stiffness varies monotonically with size, and the effective stiffnesses of two steady states are coincident. (c) The angle distributions under the two steady states have the relationship $\delta\theta_{N-n}^+ = -\delta\theta_n^-$. (d) In the even-node chain, the effective stiffness varies non-monotonically with size, and the effective stiffnesses of two steady states do not coincide, but they have the same maximum point $N_p' = 4$. (e) The even-node chains are axisymmetric (figure above). The angle distribution has the relationship $\delta\theta_n^+ = \delta\theta_{N-n}^+$ (figure below). The rotation deformation is regarded as a superposition of homogeneous deformation (C_θ , dotted line in the figure) and inhomogeneous deformation ($\delta\theta^{\text{inh}}$, light gray fill), and under the steady state $\bar{\theta} = \theta_s$ ($\bar{\theta} = -\theta_s$), C_θ and $\delta\theta^{\text{inh}}$ produce positive (negative) superposition, they are represented in the

figure by the marks “+” and “-”, respectively. (f) The eccentric excitation is equivalent to the combination of the concentrated force $F/2$ through the center and the moment $(Fl \cos \bar{\theta})/2$, where the response of $F/2$ corresponds to the homogeneous deformation (green cross), and the response of $(Fl \cos \bar{\theta})/2$ corresponds to the inhomogeneous deformation (light blue cross), and the two responses under steady state $\bar{\theta} = \theta_s$ and $\bar{\theta} = -\theta_s$ generate a superposition of type “+” and type “-”, respectively.

Different from the above case of odd nodes, the effective stiffnesses of the even-node chain do not coincide under the initial configuration $\bar{\theta} = \theta_s$ and $\bar{\theta} = -\theta_s$, as shown in Fig. 2(d). The total deformation of the chain is resolved into homogeneous deformation and inhomogeneous deformation as shown in Fig. 2(f) ([Movie S3](#) shows the homogeneous deformation of the chain, and [Movie S4](#) shows the inhomogeneous deformation of the chain under unilateral moment excitation), this non-coincidence behavior comes from the different superposition modes of these two deformation components. Specifically, the homogeneous deformation and inhomogeneous deformation under $\bar{\theta} = \theta_s$ have the same contribution to ΔL_e , as shown in Fig. 2(f) above, in this case, these two deformation components produce the positive superposition, which is represented by the mark “+” in Fig. 2(e). While under $\bar{\theta} = -\theta_s$, the contributions of the two deformation components to ΔL_e are opposite, as shown in Fig. 2(f) below, in which the two deformation components generate the negative superposition, as represented by the mark “-” in Fig. 2(e). As shown in Fig. 2(e), the different superposition modes lead to the difference between the total deformation distributions under the two initial configurations, resulting in the chain exhibiting different stiffness under two initial configurations.

In the case of even nodes, the effective stiffnesses of two steady states are not equal, but both exhibit anomalous size effects, and they have the same maximum point $N_{P'} = 4$, as shown by the gray solid line in Fig. 2(d). In other words, the chains under the two steady states have the same optimal size to achieve the maximum stiffness, this special phenomenon will be discussed in Section 3.2 based on the continuum model.

3.2. Continuum model for even nodes

For the governing equations Eqs. (2b) and (3b), the form in the continuum limit

is considered,

$$\frac{\partial^2 u}{\partial X^2} = -2\eta l \sin \bar{\theta} \frac{\partial \delta \theta}{\partial X}, \quad (6)$$

$$\frac{\partial^2 \delta \theta}{\partial X^2} - \frac{1}{(\lambda^*)^2} \delta \theta = -\frac{F\eta l \sin \bar{\theta}}{k_s l^2 \cos^2 \bar{\theta} - k_\theta}, \quad (7)$$

where,

$$\lambda^* = \sqrt{\frac{k_s l^2 \cos^2 \bar{\theta} - k_\theta}{6k_\theta - k_t(\eta l)^2 [2 \cos(2\bar{\theta}) - \beta \cos \bar{\theta}]}}. \quad (8)$$

λ^* is the characteristic decay length of the inhomogeneous deformation, which is the length required for the infinite chain to decay a unit deformation in logarithmic coordinates.

For the even-node chain, as shown in Fig. 2(e), it has axial symmetry, which simplifies the form of the angle solution, namely, $\delta \theta(X) = \delta \theta(N - X)$. The solution to Eq. (7) can be written as

$$\delta \theta = \delta \theta^{\text{inh}} + \delta \theta^{\text{h}} = C_1 [e^{X/\lambda^*} + e^{(N-X)/\lambda^*}] + C_\theta. \quad (9)$$

As can be seen from Eq. (9), unlike the monostable chain whose rotation deformation is purely composed of inhomogeneous deformation (Coulais et al., 2018), rotation deformation in the bistable chain has two parts: inhomogeneous deformation $\delta \theta^{\text{inh}} = C_1 [e^{X/\lambda^*} + e^{(N-X)/\lambda^*}]$ and homogeneous deformation $\delta \theta^{\text{h}} = C_\theta$, which correspond to the response under the moment and the concentrated force through the center in Fig. 2(f) respectively. The easily solvable C_θ is first identified, as the particular solution of Eq. (7), which can be written as

$$C_\theta = \frac{(\lambda^*)^2 F\eta l \sin \bar{\theta}}{k_s l^2 \cos^2 \bar{\theta} - k_\theta} = \frac{F\eta l \sin \bar{\theta}}{6k_\theta - k_t(\eta l)^2 [2 \cos(2\bar{\theta}) - \beta \cos \bar{\theta}]}, \quad (10)$$

on the other hand, in a physical sense, C_θ is the homogeneous rotation deformation of the chain after each node is subjected to the moment $F\eta l \sin \bar{\theta}$, which can also be directly determined by the equilibrium equation. Next, C_1 is determined by the boundary condition Eq. (3a),

$$C_1 = \frac{Fl \cos \bar{\theta}}{K_1 (1 + e^{N/\lambda^*}) - K_2 [e^{1/\lambda^*} + e^{(N-1)/\lambda^*}]}, \quad (11)$$

where, $K_1 = 4k_\theta + 2k_s l^2 \cos^2 \bar{\theta} - k_t(\eta l)^2 (2 \cos 2\bar{\theta} - \beta \cos \bar{\theta})$, $K_2 = 2(k_s l^2 \cos^2 \bar{\theta} - k_\theta)$.

Substituting Eq. (9) into Eq. (6), the displacement solution can be obtained,

$$u = u^{\text{inh}} + u^{\text{h}} + D_2 = -2\eta l \lambda^* C_1 [e^{X/\lambda^*} - e^{(N-X)/\lambda^*}] \sin \bar{\theta} - D_1 \left(X - \frac{N}{2} \right) + D_2. \quad (12)$$

Similarly, unlike the monostable chain whose displacement deformation is purely described by homogeneous deformation, due to the coupling of translation and rotation, the displacement deformation in the bistable chain has inhomogeneous deformation part $u^{\text{inh}} = -2\eta l \lambda^* C_1 [e^{X/\lambda^*} - e^{(N-X)/\lambda^*}] \sin \bar{\theta}$ and homogeneous deformation part $u^{\text{h}} = -D_1(X - N/2)$.

In Eq. (12), u^{inh} is generated by the reduction of the horizontal projection of the rigid cross after it is rotated by angle $\delta\theta^{\text{inh}}$. After each node of the chain rotates at the corresponding angle $\delta\theta^{\text{inh}}$ (namely, the n -th node rotates at the angle $\delta\theta^{\text{inh}}(n)$, $n \in [0, N]$), the displacement difference between the 0-th node and the N -th node (denoted as ΔL_0) is

$$\Delta L_0 = u^{\text{inh}}(0) - u^{\text{inh}}(N) = (\eta l \sin \bar{\theta}) \sum_0^{N-1} [\delta\theta^{\text{inh}}(n) + \delta\theta^{\text{inh}}(n+1)], \quad (13)$$

where, $\sum_0^{N-1} [\delta\theta^{\text{inh}}(n) + \delta\theta^{\text{inh}}(n+1)]$ can be obtained by summing Eqs. (3) ([see \(i\)-1 in Appendix B for details](#)), ΔL_0 can be further expressed as

$$\Delta L_0 = 2lC_\theta \cos \bar{\theta}. \quad (14)$$

The result of Eq.(14) shows that the value of $u^{\text{inh}}(0) - u^{\text{inh}}(N)$ is independent of the size N' . Namely, when the initial configuration is fixed, no matter how many nodes the chain has, the end-to-end displacement difference generated by the inhomogeneous rotation deformation is always a constant under unit force, which is the most basic anomalous property to the bistable chain. In [Movie S5](#), this anomalous property is verified by simulations.

For the homogeneous deformation part u^{h} in Eq. (12), the expression of the integral constant D_1 is

$$D_1 = 2\eta l C_\theta \sin \bar{\theta} + F / (2k_l), \quad (15)$$

where $2\eta l C_\theta \sin \bar{\theta}$ is the reduction of the horizontal projection after single cross is rotated by angle C_θ , $F / (2k_l)$ is the reduction in the length of single shim under pressure $F / 2$. D_2 corresponds to the rigid body translation mode generated by the rank-deficient matrix $[K]$ (the structure lacks a horizontal constraint), which can take any value because it is eliminated in Eq. (5). In summary, the four integral constants

in the continuum model are all determined. The complete continuum model provides a contrast to the numerical and experimental results, as shown in Fig. 2(d). Next, it will be used to analyze the maximum point of the stiffness.

In order to carry out the analysis of the maximum point more simply, the effective compliance of the chain with the initial configuration of $\bar{\theta}$ and nodes of N' is defined as $\eta_e(\bar{\theta}, N') = [k_e(\bar{\theta}, N')]^{-1}$ (see (i)-2 in Appendix B for details),

$$\eta_e(\bar{\theta}, N') = \frac{1}{F} [2\Delta L_0(\bar{\theta}) + 2l\delta\theta_0^{\text{inh}}(\bar{\theta}, N') + D_1(\bar{\theta})N], \quad (16)$$

which is the change of the equivalent pressure bar under a pair of unit forces, the definition of $\delta\theta_0^{\text{inh}}$ in Eq. (16) is $\delta\theta_0^{\text{inh}} = \delta\theta^{\text{inh}}(X) \big|_{X=0}$,

$$\delta\theta_0^{\text{inh}}(\bar{\theta}, N') = \frac{Fl \cos \bar{\theta} (1 + e^{N/\lambda^*})}{K_1 (1 + e^{N/\lambda^*}) - K_2 [e^{1/\lambda^*} + e^{(N-1)/\lambda^*}]}. \quad (17)$$

In Eq. (16), both $\delta\theta_0^{\text{inh}}(\bar{\theta})$ and $D_1(\bar{\theta})$ have even symmetry. Although $\Delta L_0(\bar{\theta})$ does not have even symmetry, it is size-independent, which makes the η_e of the even-node chain have a special property, that is, $\partial_{N'}[\eta_e(\bar{\theta}, N')] = \partial_{N'}[\eta_e(-\bar{\theta}, N')]$. This property guarantees that the stiffness curves under $\bar{\theta} = \theta_s$ and $\bar{\theta} = -\theta_s$ have the same stationary point, namely, the even-node chains under two stable states reach maximum stiffness at the same size, which explains that the two stiffness curves in 2(c) have the same maximum point.

In this section, the size independence of ΔL_0 ensures that the compliances of two steady states have the same change rate, however, the special properties based on $\Delta L_0 = 2lC_\theta \cos \bar{\theta}$ in the bistable chain are not limited to this. In ΔL_e , the inhomogeneous deformation part (denoted as ΔL_e^{inh}) and homogeneous deformation part (denoted as ΔL_e^{h}) are expressed as

$$\Delta L_e^{\text{inh}} = 2l(C_\theta + \delta\theta_0^{\text{inh}}) \cos \bar{\theta}, \quad (18)$$

$$\Delta L_e^{\text{h}} = D_1 N + 2lC_\theta \cos \bar{\theta}. \quad (19)$$

According to Eqs. (18) and (19), the anomalous size effect in Fig. 2(d) can still only be explained at the qualitative level, namely, the homogeneous deformation always increases with the increase in size, because $D_1 N$ in ΔL_e^{h} can be equivalent to the response of the system formed by N springs in series, the greater number of springs in series, the greater the response deformation; while inhomogeneous deformation reaches the maximum at the smallest even nodes $N' = 2$, which always decreases

with the increase in size (see (i)-3 in Appendix B for details), competition between the two deformation modes results in anomalous size effects. But in Eqs. (18) and (19) we note another important result, that ΔL_0 ($2lC_\theta \cos \bar{\theta}$ in both equations) makes a connection between inhomogeneous deformation and homogeneous deformation, which is different from the decoupling of inhomogeneous deformation and homogeneous deformation in the monostable chain. This connection makes quantitative analysis for the anomalous size effect possible, so in following Section 4 we attempt to quantitatively reveal the mechanism of the anomalous size effects.

4. Criticality of stiffness transition

4.1. Constant criticality for $\bar{\theta} = \theta_s$

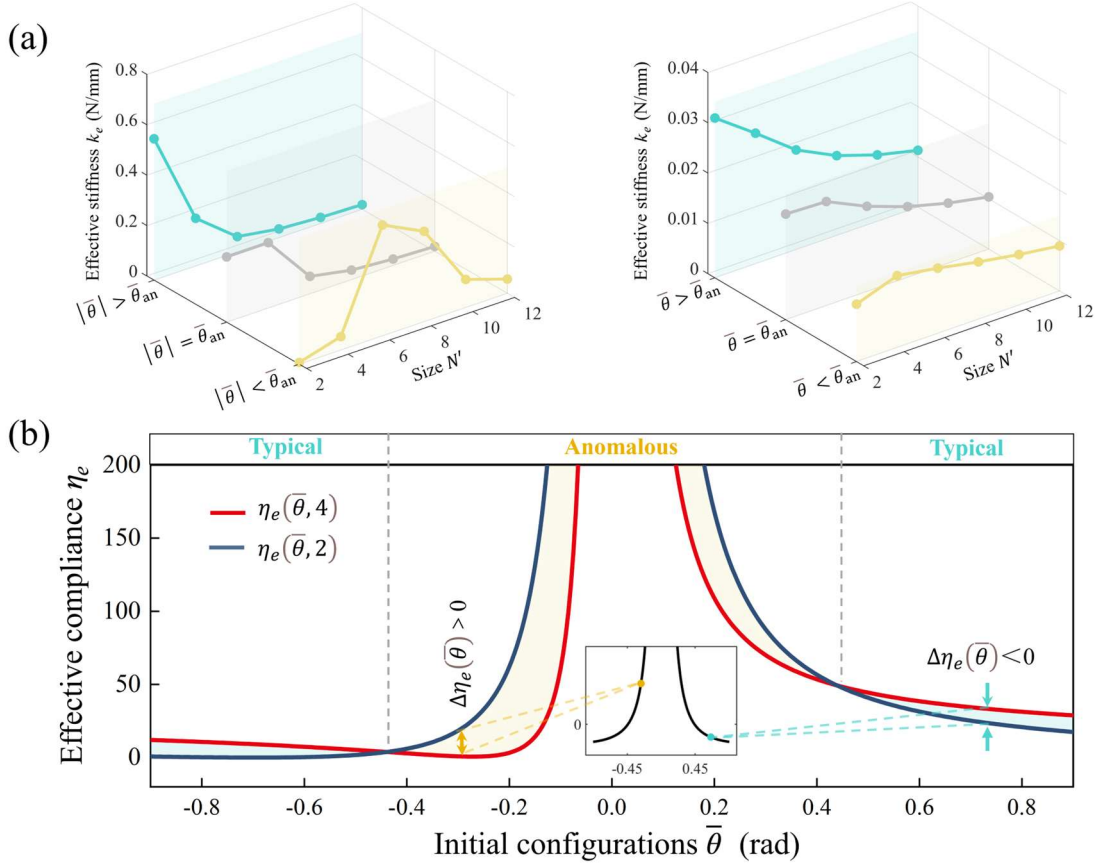


Fig. 3. (a) Size effects under different initial configurations, the monotonicity of stiffness variation can be determined by comparing the stiffness of the 2-node structure with that of the 4-node structure. (b) The compliance of the 2-node structure and the compliance of the 4-node structure vary with the initial configuration, the symmetric intersections of the two compliance curves indicate that the range with anomalous size effects is symmetrically distributed on the horizontal axis. The illustration shows the variation of the compliance difference $\Delta\eta_e(\bar{\theta}) = \eta_e(\bar{\theta}, 2) -$

$\eta_e(\bar{\theta}, 4)$ with the initial configuration, and $\Delta\eta_e(\bar{\theta})$ is even symmetric.

Before discussing the mechanism of the anomalous size effect, it is necessary to determine the range in which it occurs. As shown in Fig. 3(a), in the discrete system, if the stiffness increases first and then decreases, this requires $k_e(\bar{\theta}, 2) < k_e(\bar{\theta}, 4)$, which means that the boundary of the range in which anomalous size effect occurs can be given by $k_e(\bar{\theta}, 2) = k_e(\bar{\theta}, 4)$. The variation curves of $\eta_e(\bar{\theta}, 2)$ and $\eta_e(\bar{\theta}, 4)$ with respect to $\bar{\theta}$ are shown in Fig. 3(b), which shows that the initial configuration with the anomalous size effect has a symmetric range $[-\bar{\theta}_{\text{an}}, \bar{\theta}_{\text{an}}]$, $\bar{\theta}_{\text{an}} = 0.45$ (rad). The source of this symmetry is explained below. Although $\eta_e(\bar{\theta}, N')$ does not have any symmetry, in the compliance difference between the 2-node structure and the 4-node structure ($\Delta\eta_e(\bar{\theta}) = \eta_e(\bar{\theta}, 2) - \eta_e(\bar{\theta}, 4)$), the ΔL_0 without even symmetry is eliminated in the compliance difference due to its size-independence. Therefore, $\Delta\eta_e(\bar{\theta})$ is even symmetric, as shown in the illustration of Fig. 3(b), which results in the range of the anomalous size effect being symmetrically distributed along the horizontal axis.

Further, we discuss the criticality at which stiffness monotonicity transitions, and the case of $\bar{\theta} = \theta_s$ is discussed first. An inhomogeneity index P reflecting the proportion of inhomogeneous deformation is defined,

$$P = \text{sgn} \left(\frac{\Delta L_e^{\text{inh}}}{\Delta L_e^{\text{h}}} \right) \frac{|\Delta L_e^{\text{inh}}|}{|\Delta L_e^{\text{inh}}| + |\Delta L_e^{\text{h}}|}, \quad (20)$$

$P \in [-1, 1]$, $|P| \rightarrow 1$ and $|P| \rightarrow 0$ correspond to inhomogeneous deformation and homogeneous deformation dominating in total deformation, respectively. In addition, $P > 0$ indicates that inhomogeneous deformation and homogeneous deformation produce positive superposition, and $P < 0$ indicates that they produce negative superposition. Fig. 4(a) shows the P -values under different initial configurations and sizes, the variation trend of index P indicates that the proportion of inhomogeneous deformation decreases with the increase of initial angle and size. In order to explore the relationship between P -values and stiffness monotonicity, under each initial configuration, the derivative of stiffness with respect to size (dk_e / dN') is plotted in Fig. 4(b), where the yellow (baby blue) region represents the increasing (decreasing) interval of stiffness. These two regions are separated by the white region

between them, the white region is the criticality at which the stiffness monotonicity transitions. When the curve $P(\bar{\theta}, N') = 0.5$ in Fig. 4(a) is plotted to Fig. 4(b), we find that the curve is located in the white region separating the increasing and decreasing interval, which indicates that the relationship between the proportion of inhomogeneous deformation and stiffness monotonicity can be quantified. For the case of $|\bar{\theta}| < \bar{\theta}_{\text{an}}$, when the proportion of inhomogeneous deformation is higher than 0.5 (namely, at small sizes), the stiffness increases with the increase in size. If the size continues to increase, the proportion of inhomogeneous deformation will be lower than 0.5, and the stiffness will decrease with the increase in size. The above discussion reinterprets the anomalous size effect at a quantitative level and concludes that the stiffness monotonicity follows $P = 0.5$ as the transition criticality.

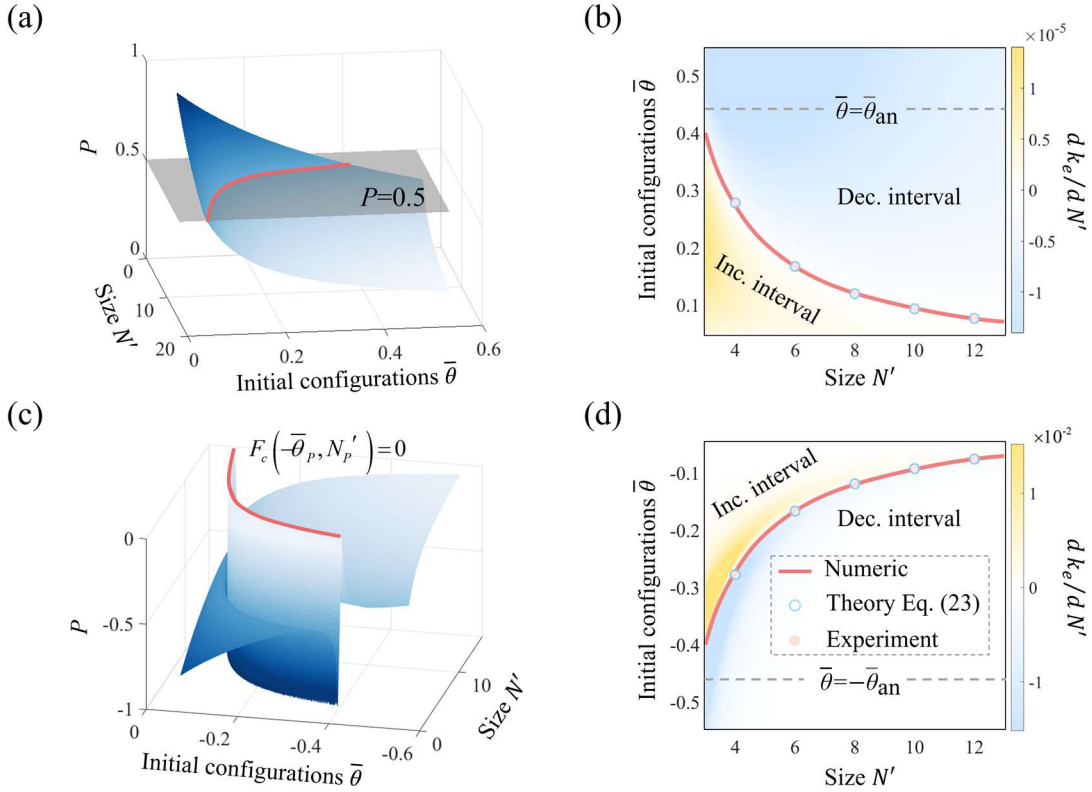


Fig. 4 (a) In the case of $\bar{\theta} = \theta_s$, the variation of inhomogeneity index P with respect to initial configuration and size, the pink solid line in the figure is the curve $P(\bar{\theta}, N') = 0.5$. (b) A phase diagram about the derivative of stiffness with respect to size (dk_e/dN') under each initial configuration, where the increasing interval and decreasing interval of $k_e(N')$ are separated by the curve $P(\bar{\theta}, N') = 0.5$. (c) In the case of $\bar{\theta} = -\theta_s$, the P -values surface is discontinuous, and the pink solid line $F_c(-\bar{\theta}_p, N_p') = 0$ is obtained by fitting the discontinuity points. (d) A phase

diagram of the derivative, the curve $F_c(-\bar{\theta}_P, N_{P'}) = 0$ separates the increasing and decreasing interval of stiffness. The azure hollow circle in the figure is the result of Eq. (23), under the initial configuration corresponding to the azure hollow circle, the experimental results of the maximum point $N_{P'}$ are shown in the light pink dot in the figure.

4.2. Oscillating criticality for $\bar{\theta} = -\theta_s$

As shown in Fig. 4(c), for the case of $\bar{\theta} = -\theta_s$, $P < 0$, which indicates that there is a cancellation between the inhomogeneous and homogeneous deformation. In Fig. 4(c), the P -values surface in this case is not continuous like the surface under $\bar{\theta} = \theta_s$, and the oscillating discontinuity point occurs as P tends to -0.5 . These discontinuity points are projected onto the $\bar{\theta} - N'$ plane and fitted into a continuous curve, as shown by the pink curve in Fig. 4(c), when this curve is drawn into the derivative phase diagram, it also exactly separates the increasing and decreasing interval of stiffness, as shown in Fig. 4(d). We note that this singular P -values seems to be different from the previous cognition to the origin of anomalous size effects, namely, the anomalous size effect comes from the competition between the inhomogeneous and homogeneous deformation, and it also does not follow the conclusion in Section 4.1 that $P = 0.5$ is the criticality. This singular phenomenon has caught our attention, and this phenomenon will be discussed in detail next.

The curve obtained by fitting is denoted as $F_c(-\bar{\theta}_P, N_{P'}) = 0$. According to the expression for P , when $(\bar{\theta}, N') \rightarrow (-\bar{\theta}_P, N_{P'})$, the oscillating discontinuous point can only occur when ΔL_e^{inh} and ΔL_e^{h} approach 0 at the same time, which requires curve $\Delta L_e^{\text{inh}}(\bar{\theta}, N') = 0$ and curve $\Delta L_e^{\text{h}}(\bar{\theta}, N') = 0$ to almost coincide, and in Fig. 4(c), $\Delta L_e^{\text{inh}}(\bar{\theta}, N') = 0$ and $\Delta L_e^{\text{h}}(\bar{\theta}, N') = 0$ correspond to the curve connected by discontinuous point of $P = -1$ and $P = 0$, respectively. Next, we will combine the numerical results to prove that this coincidence is possible, and that it is closely related to the basic property that $\Delta L_0 = 2lC_\theta \cos \bar{\theta}$.

According to Eq. (18), let $\Delta L_e^{\text{inh}} = 0$ to get the condition that inhomogeneous deformation equals 0, namely, $\delta\theta_0^{\text{inh}} = -C_\theta$. Substituting Eqs. (10) and (17) into this condition,

$$-\frac{1}{\eta \tan \bar{\theta}} = \frac{(K_1 - K_2)\tilde{\delta}\theta^{\text{inh}}(0) - K_2[\tilde{\delta}\theta^{\text{inh}}(1) - \tilde{\delta}\theta^{\text{inh}}(0)]}{(K_1 - K_2)\tilde{\delta}\theta^{\text{inh}}(0)}, \quad (21)$$

where, $\tilde{\delta}\theta^{\text{inh}}(X) = e^{X/\lambda^*} + e^{(N-X)/\lambda^*}$ is the normalized inhomogeneous angle distribution. Next, the condition for homogeneous deformation ΔL_e^h equal to 0 is discussed. Because the chain is connected through the low torsional shims, $2\eta l C_\theta \sin \bar{\theta} \gg F / (2k_l)$ in D_1 , namely, the tension deformation of the shim can be ignored (Tang et al., 2023). So ΔL_e^h is approximated as

$$\Delta L_e^h \approx 2l C_\theta (\eta N \sin \bar{\theta} + \cos \bar{\theta}), \quad (22)$$

the condition for $\Delta L_e^h = 0$ can be written as

$$-\frac{1}{\eta \tan \bar{\theta}} = N. \quad (23)$$

The left term of Eqs. (21) and (23) are the same, so the right term of Eq. (21) is simplified. $\tilde{\delta}\theta^{\text{inh}}(X)$ satisfies the homogeneous form of Eq. (7),

$$\frac{K_2}{2} \frac{\partial^2 [\tilde{\delta}\theta^{\text{inh}}(X)]}{\partial X^2} = (K_1 - K_2)\tilde{\delta}\theta^{\text{inh}}(X). \quad (24)$$

$\partial_{XX}\tilde{\delta}\theta^{\text{inh}}|_{X=i} = \partial_X\tilde{\delta}\theta^{\text{inh}}|_{X=i} - \partial_X\tilde{\delta}\theta^{\text{inh}}|_{X=i-1}$, this backward difference form is considered, $\partial_{XX}\tilde{\delta}\theta^{\text{inh}}$ and $\partial_X\tilde{\delta}\theta^{\text{inh}}$ have the following relationship,

$$\sum_{i=1}^N \frac{\partial^2 \tilde{\delta}\theta^{\text{inh}}}{\partial X^2} \Big|_{X=i} = \sum_{i=1}^N \left(\frac{\partial \tilde{\delta}\theta^{\text{inh}}}{\partial X} \Big|_{X=i} - \frac{\partial \tilde{\delta}\theta^{\text{inh}}}{\partial X} \Big|_{X=i-1} \right) = -2 \frac{\partial \tilde{\delta}\theta^{\text{inh}}}{\partial X} \Big|_{X=0}, \quad (25)$$

the last step of Eq. (25) uses symmetry $\partial_X\tilde{\delta}\theta^{\text{inh}}|_{X=0} = -\partial_X\tilde{\delta}\theta^{\text{inh}}|_{X=N}$. Using Eq. (24) to replace $\partial_{XX}\tilde{\delta}\theta^{\text{inh}}$ in Eq. (25), the relationship between $\partial_X\tilde{\delta}\theta^{\text{inh}}$ and $\tilde{\delta}\theta^{\text{inh}}(X)$ is established,

$$\sum_{i=1}^N (K_1 - K_2)\tilde{\delta}\theta^{\text{inh}}(i) = -K_2 \frac{\partial \tilde{\delta}\theta^{\text{inh}}}{\partial X} \Big|_{X=0}. \quad (26)$$

$\tilde{\delta}\theta^{\text{inh}}(1) - \tilde{\delta}\theta^{\text{inh}}(0)$ in Eq. (21) is expanded to a second-order form,

$$\tilde{\delta}\theta^{\text{inh}}(1) - \tilde{\delta}\theta^{\text{inh}}(0) = \frac{\partial \tilde{\delta}\theta^{\text{inh}}}{\partial X} \Big|_{X=0} + \frac{1}{2} \frac{\partial^2 \tilde{\delta}\theta^{\text{inh}}}{\partial X^2} \Big|_{X=0}. \quad (27)$$

Substituting orderly Eq. (27) and Eq. (26) into the numerator in the right term of Eq. (21) leads to

$$(K_1 - K_2)\tilde{\delta}\theta^{\text{inh}}(0) - K_2[\tilde{\delta}\theta^{\text{inh}}(1) - \tilde{\delta}\theta^{\text{inh}}(0)] = -K_2 \frac{\partial \tilde{\delta}\theta^{\text{inh}}}{\partial X} \Big|_{X=0} = (K_1 - K_2) \sum_{i=1}^N \tilde{\delta}\theta^{\text{inh}}(i). \quad (28)$$

In the first step of Eq. (28), $(K_1 - K_2)\tilde{\delta\theta}^{\text{inh}}(0)$ is eliminated by $(K_2 / 2)\partial_{XX}\tilde{\delta\theta}^{\text{inh}}|_{X=0}$, where the relationship $(K_1 - K_2)\tilde{\delta\theta}^{\text{inh}}(0) - (K_2 / 2)\partial_{XX}\tilde{\delta\theta}^{\text{inh}}|_{X=0} = 0$ is obtained based on Eq. (24). For $\sum_{i=1}^N \tilde{\delta\theta}^{\text{inh}}(i)$ in Eq. (28), it is represented as

$$\sum_{i=1}^N \tilde{\delta\theta}^{\text{inh}}(i) = N\tilde{\delta\theta}^{\text{inh}}(0) + \sum_{i=1}^N [\tilde{\delta\theta}^{\text{inh}}(i) - \tilde{\delta\theta}^{\text{inh}}(0)]. \quad (29)$$

In Eq. (29), the relative error generated when $\sum_{i=1}^N \tilde{\delta\theta}^{\text{inh}}(i)$ approximates $N\tilde{\delta\theta}^{\text{inh}}(0)$ is

$$\mu = \frac{\sum_{i=1}^N |\tilde{\delta\theta}^{\text{inh}}(i) - \tilde{\delta\theta}^{\text{inh}}(0)|}{\sum_{i=1}^N |\tilde{\delta\theta}^{\text{inh}}(i)|} \times 100\%. \quad (30)$$

Substituting Eq. (28) and $\sum_{i=1}^N \tilde{\delta\theta}^{\text{inh}}(i) = N\tilde{\delta\theta}^{\text{inh}}(0)$ into Eq. (21) in turn yields the curve $N + (\eta \tan \bar{\theta})^{-1} = 0$ (namely, Eq. (23)), while the relative error μ is given on this curve. According to numerical results in Fig. 4(c) and Fig. 4(d), this curve (namely, the curve $P(\bar{\theta}, N') = -1$ corresponding to Eq. (23)) has the attribute of separating the increasing and decreasing interval, based on which the relative error μ is calculated. Taking the chain we selected as an example, the results in Fig. 2(d) show that the stiffness monotonicity transitions when the size N' is 4. Combined with the inhomogeneous angle distribution of the 4-node structure shown in Fig. 2(e), although the decay factor q ($q = \exp(-1/\lambda^*)$) at this time is 0.8, the decayed rotation deformation at both ends produces an obvious superposition, which significantly reduces the decay speed of the decay deformation at both ends. Therefore, due to the existence of superposition effects, the inhomogeneous deformation formed by superposition at transition size has almost no decay. For the case where the transition size is 4, the relative error is only 2.8%. In fact, for a smaller transition size, the relative error will be smaller due to decay deformation producing a more significant superposition; for a larger transformation size, the decay speed of the decay deformation itself decreases ([see \(i\)-3 in Appendix B for details](#)), which makes the relative error close to or even smaller than 2.8%. In summary, smaller errors indicate that Eq. (23) can be used as an approximate solution for Eq. (21), which proves that the conditions for inhomogeneous deformation and homogeneous deformation equal to 0 are almost identical, resulting in the oscillation of P -values. In addition, we point out that $q = 0.8$ is not a special value set in order for the $\sum_{i=1}^N \tilde{\delta\theta}^{\text{inh}}(i) \approx N\tilde{\delta\theta}^{\text{inh}}(0)$

to hold, but rather a moderate value for anomalous size effects. Because if the decay factor q approaches 0, namely, the decay speed is very fast, the shift of $N_{P'}$ to the left will eventually result in anomalous size effects not being observed in discrete or real systems. Therefore, only the deformation mode with low enough energy can ensure the appearance of the anomalous size effect, which often requires smaller non-zero k_θ (namely, larger q).

In the above proof, Eq. (23) gives the most concise relationship between the transformation size and the initial configuration ($N_{P'} = -(\eta \tan \bar{\theta})^{-1} + 1$), which is drawn in by hollow circles in Fig. 4(d). The good agreement between the circle and the solid line confirms the correctness of the above theoretical analysis. In the experiment, by adjusting the original length of the spring, the initial configuration is consistent with the ordinate of the hollow circle. The stiffnesses at each size are measured under this initial configuration, and the size corresponding to the maximum stiffness is shown by the light pink dots in Fig. 4(d).

Eq. (23) also reveals another unusual property of bistable chains, that is, the transition size $N_{P'}$ is only dependent on the initial configuration and the shim length, neither the stiffness parameters of the shim nor the stiffness of the spring can change the value of $N_{P'}$. This anomalous effect is significantly different from the anomalous effects in the monostable chain, where the stiffness parameters of the flexible hinge will change the value of $N_{P'}$ (Coulais et al., 2018). The $N_{P'}$ of a bistable chain is related to only two physical quantities that describe the geometric relationship, which makes the design and customization of anomalous size effects easier. In addition, notably, Eq. (23) indicates that longer shims reduce $N_{P'}$. This may seem to be the opposite of the relationship between $N_{P'}$ and hinge length in the monostable chain, but in fact, the two are not in conflict. η in Eq. (23) comes from $\eta l \sin \bar{\theta}$ in Eq. (2), and η in Eq. (2) takes on the role of describing the geometric relationship of the shim. The longer the shim, the greater the end-to-end displacement caused by C_θ , where ΔL_e^h reaches 0 at the shorter nodes, resulting in the left shift of $N_{P'}$. However, in the monostable chain, l_h plays the role of describing the equivalent stiffness of the flexible hinges. If l_h becomes larger, intuitively it leads to a decrease in k_θ (more specifically, it leads to a decrease in k_θ / k_s), and an increase in λ^* ($\lambda^* \sim \sqrt{k_s / k_\theta}$) causes the right shift of $N_{P'}$. Thus, l_h assumes different roles in the two kinds of chains, making it exhibit opposite effects on $N_{P'}$.

In addition to giving the relation Eq. (23), the above demonstration also shows that the oscillating P -value corresponds to that the inhomogeneous and homogeneous deformation can simultaneously approach 0, namely, ΔL_e ($\Delta L_e = \Delta L_e^{\text{inh}} + \Delta L_e^{\text{h}}$) can approach to 0. In the case where the compliance can go to 0, the maximum stiffness must occur at the point where the compliance tends to 0. Therefore, the curve obtained by connecting the discontinuity points must separate the increasing and decreasing interval, which provides a theoretical explanation for the stiffness taking P -values oscillation as the transition criticality under $\bar{\theta} = -\theta_s$. We show that this discussion about oscillating criticality can also provide an intuitive explanation for the constant criticality under $\bar{\theta} = \theta_s$. Based on the relation in Section 3 that the stiffnesses of the two steady states have the same maximum point, the transition points for $\bar{\theta} = \theta_s$ and $\bar{\theta} = -\theta_s$ are denoted respectively as $(\bar{\theta}_s, N_{P'})$ and $(-\bar{\theta}_s, N_{P'})$. When $\Delta L_e^{\text{inh}}(-\bar{\theta}_s, N_{P'}) = 0$ and $\Delta L_e^{\text{h}}(-\bar{\theta}_s, N_{P'}) = 0$ are both satisfied, according to Eqs. (18) and (22),

$$\Delta L_e^{\text{inh}}(\bar{\theta}_s, N_{P'}) = \Delta L_e^{\text{h}}(\bar{\theta}_s, N_{P'}) = 2\Delta L_0. \quad (31)$$

Eq. (31) shows that when the structure size is $N_{P'}$, its inhomogeneous deformation is equal to its homogeneous deformation, namely, $P = 0.5$, which explains the constant criticality under $\bar{\theta} = \theta_s$, and this critical constant can only be 0.5, its value is not affected by the parameters of the shim and the initial configuration.

In this section, two kinds of criticalities correspond to two mechanisms for achieving the anomalous size effect. The one is the competition mechanism that can be characterized by the proportion of inhomogeneous deformation. The other is the cancellation mechanism, which is a mechanism by which the cancellation between the two kinds of deformation and the cancellation within them are hybridized, this cancellation mechanism is a new mechanism unique to bistable chains. For the anomalous size effect achieved by this cancellation mechanism, it should be noted that, since the k_l of the shim is not infinite in reality, the tension deformation in Eq. (22) cannot be completely ignored. Therefore, the maximum stiffness under $\bar{\theta} = -\theta_s$ cannot reach infinity, such as $k_e(N')|_{N'=4}$ in Fig. 2(d) below. However, although the stiffness has an upper bound, the relationship that k_l is much greater than k_s and $k_\theta l^{-2}$ is guaranteed by the flexible hinge, which makes the stiffness of the 4-node structure much larger than otherwise. This feature is obviously different from the flat

stiffness curve under the competition mechanism, as shown in Fig. 2(d). In the following study in Section 5, the loading force is further increased. We will further discuss the difference in the two kinds of mechanisms under nonlinear large deformation.

5. Robust anomalous size effect

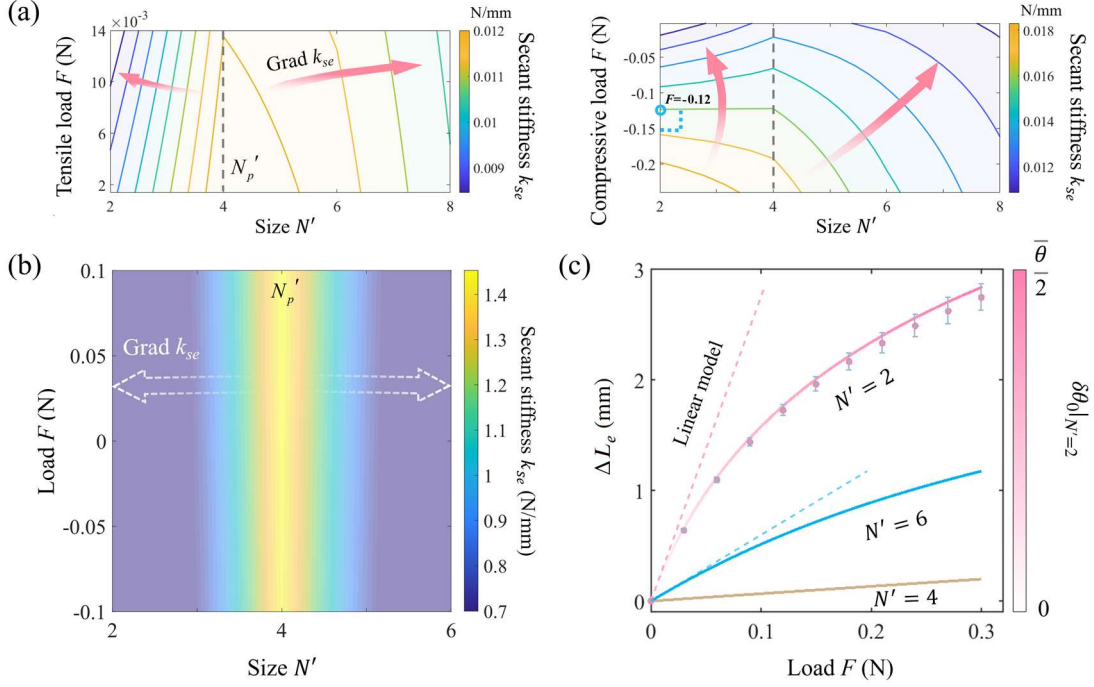


Fig. 5 (a) Stiffness contour diagram under the steady state $\bar{\theta} = \theta_s$, where the positive and negative signs of the vertical axis F respectively indicate that the structure is subjected to tension and pressure. The distribution of contour is affected by the type and magnitude of load F , in particular, the contour is perpendicular to the vertical axis when $F = -0.12$ N. (b) Stiffness contour diagram under the steady state $\bar{\theta} = -\theta_s$, the distribution of contours is almost unaffected by the load F . (c) $F - \Delta L_e$ curves of $N' = \{2, 4, 6\}$, where the color of the curve for $N' = 2$ indicates the magnitude of the rotational deformation.

From the perspective of structural response, the anomalous size effect can be described as: when the excitation F is fixed, the chain structure with more nodes has a smaller end-to-end displacement ΔL_e . In the linear case discussed in the previous section, the displacement ΔL_e can be expressed as $\Delta L_e = (1 / k_e)F$. When a definite pair of F is applied to both ends of the structure, the structure with greater stiffness k_e will yield a smaller ΔL_e . Therefore, in the previous section, when the stiffness of the large-size structure is larger than that of the small-size structure, the

large-size structure has a smaller response, and the size effect of the structure is anomalous. In nonlinear large deformation, this scheme of size-displacement is continued to be used. The difference is that the secant stiffness (k_{se}) is used to characterize this size-deformation behavior under large deformation, because when F is fixed, secant stiffness k_{se} can also reflect the magnitude of ΔL_e ($\Delta L_e = (1 / k_{se})F$). Similarly, the anomalous size effect occurs when the secant stiffness of the large-size structure is greater than that of the small-size structure, because then the large-size structure has a smaller response.

In Fig. 5, we use the same initial configuration as in Fig. 2, where $N_{p'} = 4$. Fig. 5(a) shows the evolution of the anomalous size effect based on competition mechanism under tensile and compressive loads. In the case of tension, with the increase of F , the denser contours indicate that the variation trend of stiffness curve becomes steeper (the stiffness curve is obtained by transversal of fixed F and surface $k_{se}(N', F)$), the non-monotonic variation of stiffness is more obvious. In the case of compression, with the increase of $-F$, the contours become sparser, the stiffness curve becomes flatter, and as the curve flattens out, the gap between $k_{se}(N')|_{N'=2}$ and $k_{se}(N')|_{N'=4}$ gradually narrows. Taking the contour perpendicular to the vertical axis as the boundary, the anomalous size effect disappears when $-F > 0.12$ N. Therefore, the results of Fig. 5(a) show that this anomalous size-deformation behavior achieved by the competition mechanism is very sensitive to the type and magnitude of the load (or the nonlinear effect).

Fig. 5(b) shows the evolution of the anomalous size-deformation behavior based on the cancellation mechanism. The results in the figure indicate that the anomalous behavior achieved by this new mechanism has strong robustness in nonlinear large deformation, which is shown by the maximum and the maximum point of stiffness are almost unaffected by the type and magnitude of loads. For the source of this robustness, it is analyzed in the next paragraph.

In the previous discussion, for the chain of $\bar{\theta} = -\theta_s$, the stiffness at $N' = 4$ is much greater than that in other cases, which makes the excitation required for the 4-node structure to enter the geometric nonlinear stage much greater than that of the structure with $N' \neq 4$. As an example, we plot the $F - \Delta L_e$ curve for the 2~6-node structure in Fig. 5(c). As can be seen from the figure, while the 2-node and 6-node structures have produced significant nonlinear large deformation, the 4-node

structures are still in the linear elastic stage. When the size effect is discussed under nonlinear large deformation, the selection of F should ensure that the deformation of the softest structure is within a reasonable range. Therefore, under such a F , the secant stiffness k_{se} of the 4-node structure (or the structure whose deformation is completely cancelled out) hardly changes with the F value. At the same time, the extremely large stiffness also means that the displacement response generated by the structure whose deformation is completely cancelled out is always the smallest, namely, the anomalous size-deformation behavior achieved by the cancellation mechanism is much more robust than that achieved by the competition mechanism.

6. Conclusions

In this work, anomalous size effects in bistable chains are systematically discussed. In a bistable chain, even in the case of linear small deformation, its translation and rotation are also coupled (more specifically, the angle is the differential of displacement), which gives the bistable chain an anomalous property — the end-to-end displacement difference caused by the decaying low-energy deformation is size-independent. This anomalous property not only makes the compliance of two steady states have the same change rate, but also establishes a connection between inhomogeneous deformation and homogeneous deformation, thus promoting the quantitative analysis of the anomalous size effect. In quantitative analysis, the proportion of inhomogeneous deformation faithfully reflects the monotonicity of stiffness, and the anomalous size effect has a constant or oscillating criticality under any initial configuration and material parameter. These two criticalities provide quantitative criteria for designing anomalous size effects in bistable chains. Even if they fail in the monostable case, Eq. (23) consistently gives the relationship between N_p' and $\bar{\theta}$ in monostable and bistable chains with low-torsion hinges, because Eq. (23) diverges at $\bar{\theta} = 0$, which corresponds exactly to the result of the monostable chain after the tensile interactions are prevented (Coulais et al., 2018), namely, the stiffness does not decrease.

In addition, in the aspect of expanding the anomalous size effects, the

cancellation mechanism makes it possible to combine this anomalous size-deformation behavior and nonlinearity robustly. But more importantly, for this class of anomalous size-deformation behavior that occurs at small sizes (such as the nanocrystalline metals (Schiøtz et al., 1998, Peng et al., 2022) and laminated beams (Wheel et al., 2015) soften as the size decreases), the cancellation mechanism or the singular case provides a new consideration besides the competition mechanism.

Acknowledgments

This work was supported by National Natural Science Foundation of China (No. 12172183), National Key Research and Development Program of China (No. 2023YFE0111000), the Natural Science Foundation of Zhejiang Province (No. LZ24A020001), International Science and Technology Cooperation Project launched by Science and Technology Bureau of Ningbo City, Zhejiang Province, China (No. 2023H011), One health Interdisciplinary Research Project (No. HY202206), Ningbo University.

Appendix A. Governing equations

The elastic potential energy of a one-dimensional chain is

$$\begin{aligned}
 E = & \sum_{n=0}^{N-1} k_l \{ u_{n+1} - u_n + \eta l [2 \cos \bar{\theta} - \cos(\bar{\theta} + \delta\theta_n) - \cos(\bar{\theta} + \delta\theta_{n+1})] \}^2 \\
 & + \sum_{n=0}^{N-1} \left\{ k_s l^2 [\sin(\bar{\theta} + \delta\theta_{n+1}) - \sin(\bar{\theta} + \delta\theta_n)]^2 + k_\theta (\delta\theta_n + \delta\theta_{n+1} + 2\bar{\theta})^2 \right\} \quad (\text{A.1}) \\
 & + \sum_{n=0}^N \frac{1}{2} a_n \left\{ k_\theta (2\delta\theta_n + 2\bar{\theta})^2 + k_t (\eta l)^2 [2 \cos(\bar{\theta} + \delta\theta_n) - \beta]^2 \right\},
 \end{aligned}$$

where, $[a_0, a_1, \dots, a_n, \dots, a_1, a_N] = [1/2, 1, \dots, 1, \dots, 1, 1/2]$. Linear small deformation cases are considered, $\delta\theta_n \ll \bar{\theta}$, the $\sin(\bar{\theta} + \delta\theta_n)$ and $\cos(\bar{\theta} + \delta\theta_n)$ in Eq. (A.1) are simplified as follows,

$$\sin(\bar{\theta} + \delta\theta_n) = \sin \bar{\theta} + \delta\theta_n \cos \bar{\theta} + o(\delta\theta_n), \quad (\text{A.2a})$$

$$\cos(\bar{\theta} + \delta\theta_n) = \cos \bar{\theta} - \delta\theta_n \sin \bar{\theta} + o(\delta\theta_n), \quad (\text{A.2b})$$

the simplified elastic potential energy is

$$\begin{aligned}
 E_{\text{lin}} = & \sum_{n=0}^{N-1} k_l [u_{n+1} - u_n + \eta l \sin \bar{\theta} (\delta\theta_n + \delta\theta_{n+1})]^2 \\
 & + \sum_{n=0}^{N-1} \left\{ k_s l^2 (\delta\theta_{n+1} - \delta\theta_n)^2 \cos^2 \bar{\theta} + k_\theta (\delta\theta_n + \delta\theta_{n+1} + 2\bar{\theta})^2 \right\} \quad (\text{A.3}) \\
 & + \sum_{n=0}^N \frac{1}{2} a_n \left\{ k_\theta (2\delta\theta_n + 2\bar{\theta})^2 + k_t (\eta l)^2 [2 \cos(\bar{\theta} + \delta\theta_n) - \beta]^2 \right\}.
 \end{aligned}$$

The relative displacement ΔL_e in Fig. 1(d) is connected with the displacement and rotation angle at both ends by the geometric constraint $c = 0$, where

$$c = \Delta L_e + u_N - u_0 - l (\delta\theta_0 \pm \delta\theta_N) \cos \bar{\theta}, \quad (\text{A.4})$$

“+” and “-” correspond to the cases of even and odd nodes, respectively. Under the constraint $c = 0$, the Lagrange function is constructed as,

$$L = E_{\text{lin}} + Fc, \quad (\text{A.5})$$

where F is the Lagrange multiplier, which corresponds to the pressure in Fig. 1(d). The equilibrium equation of the system is obtained when the objective function E_{lin} reaches its minimum under geometric constraints. $\partial L / \partial u_n = 0$ to obtain the translational governing equation Eqs. (2), and $\partial L / \partial \delta\theta_n = 0$ to obtain the rotational governing equation. In $\partial L / \partial \delta\theta_n$, the term with coefficients k_l is simplified as follows,

$$k_t [u_{n+1} - u_n + \eta l \sin \bar{\theta} (\delta\theta_n + \delta\theta_{n+1})] = -\frac{F}{2}, \quad (\text{A.6})$$

Eq. (A.6) is obtained by the force balance of each cross in the horizontal direction.

The term with coefficients k_t is simplified as follows,

$$\begin{aligned} & -k_t(\eta l)^2 [2 \cos(\bar{\theta} + \delta\theta_n) - \beta] \sin(\bar{\theta} + \delta\theta_n) \\ &= -k_t(\eta l)^2 [2 \cos(\bar{\theta} + \delta\theta_n) - \beta] \sin(\bar{\theta} + \delta\theta_n) + 6k_\theta \bar{\theta} - 6k_\theta \bar{\theta} \\ &= -k_t(\eta l)^2 \{ \sin(2\bar{\theta} + 2\delta\theta_n) - \sin(2\bar{\theta}) + [\sin \bar{\theta} - \sin(\bar{\theta} + \delta\theta_n)] \beta \} - 6k_\theta \bar{\theta} \\ &= -k_t(\eta l)^2 [2 \cos(2\bar{\theta}) - \beta \cos \bar{\theta}] \delta\theta_n - 6k_\theta \bar{\theta} + o(\delta\theta_n), \end{aligned} \quad (\text{A.7})$$

where, the transformation of $6k_\theta \bar{\theta}$ in the second step is obtained by the initial equilibrium equation $6k_\theta \bar{\theta} = k_t(\eta l)^2 [\sin(2\bar{\theta}) - \beta \sin \bar{\theta}]$. After being simplified by Eq.

(A.6) and Eq. (A.7), $\partial L / \partial \delta\theta_n = 0$ finally gives the governing equation Eqs. (3). Eqs.

(2) and (3) are written in matrix form,

$$\begin{bmatrix} -F/2 \\ Fl(\eta \sin \bar{\theta} + \cos \bar{\theta})/2 \\ \vdots \\ 0 \\ F\eta l \sin \bar{\theta} \\ \vdots \\ F/2 \\ Fl(\eta \sin \bar{\theta} \pm \cos \bar{\theta})/2 \end{bmatrix} = [\mathbf{K}] \begin{bmatrix} u_0 \\ \delta\theta_0 \\ \vdots \\ u_n \\ \delta\theta_n \\ \vdots \\ u_{N'} \\ \delta\theta_{N'} \end{bmatrix}, \quad (\text{A.8})$$

where,

$$[\mathbf{K}] = \begin{bmatrix} -k_l & k_l \eta l \sin \bar{\theta} & k_l & k_l \eta l \sin \bar{\theta} & 0 & \dots & 0 & \dots & 0 \\ 0 & a_{1,1} & 0 & a_{1,2} & 0 & \dots & 0 & \dots & 0 \\ \vdots & & \ddots & & & & \ddots & & \vdots \\ 0 & \dots & k_l & -k_l \eta l \sin \bar{\theta} & -2k_l & 0 & k_l & k_l \eta l \sin \bar{\theta} & \dots & 0 \\ 0 & \dots & 0 & a_{n,n-1} & 0 & a_{n,n} & 0 & a_{n,n+1} & \dots & 0 \\ \vdots & & \ddots & & & & \ddots & & \vdots \\ 0 & \dots & 0 & & \dots & 0 & k_l & -k_l \eta l \sin \bar{\theta} & -k_l & -k_l \eta l \sin \bar{\theta} \\ 0 & \dots & 0 & & \dots & 0 & 0 & a_{N',N'-1} & 0 & a_{N',N'} \end{bmatrix}$$

and

$$\begin{aligned} a_{1,1} &= a_{N',N'} = 2k_\theta + k_s l^2 \cos^2 \bar{\theta} - (k_t/2)(\eta l)^2 [2 \cos(2\bar{\theta}) - \beta \cos \bar{\theta}], \\ a_{n,n-1} &= a_{n,n+1} = k_\theta - k_s l^2 \cos^2 \bar{\theta}, \text{ for } n \in [1, N'], \\ a_{n,n} &= 4k_\theta + 2k_s l^2 \cos^2 \bar{\theta} - k_t(\eta l)^2 [2 \cos(2\bar{\theta}) - \beta \cos \bar{\theta}], \text{ for } n \in [2, N]. \end{aligned}$$

Eq. (A.8) abbreviated as $[\mathbf{F}] = [\mathbf{K}][\mathbf{U}]$, where $[\mathbf{F}]$ is the matrix composed of external forces, $[\mathbf{U}]$ is the matrix composed of angles and displacements, and $[\mathbf{K}]$ is the total rigid matrix of the finite chain with N' nodes. After obtaining the solution of Eq. (A.8), the end-to-end displacement is given by constraint $c = 0$,

$$\Delta L_e = u_0 - u_N + l(\delta\theta_0 \pm \delta\theta_N)\cos\bar{\theta}, \quad (\text{A.9})$$

Appendix B. Supplement to the continuum model

(i) Supplement of the continuum model for even-node

In the (i) section, we supplement some details of the continuum model for even-node, which mainly includes three parts: (i)-1 Solution for ΔL_0 , (i)-2 Solution for η_e and (i)-3 Monotonicity of $\delta\theta_0^{\text{inh}}(N')$.

(i)-1 Solution for ΔL_0

Substituting equation $\delta\theta(X) = \delta\theta^{\text{inh}}(X) + C_\theta$ into Eqs. (3), the moment term $F\eta l \sin\bar{\theta}$ in Eqs. (3) can be eliminated by C_θ , and the governing equation of inhomogeneous deformation is finally obtained,

$$\begin{aligned} (Fl \cos\bar{\theta}) / 2 &= k_\theta(\delta\theta_1^{\text{inh}} + 2\delta\theta_0^{\text{inh}}) - k_s l^2 (\delta\theta_1^{\text{inh}} - \delta\theta_0^{\text{inh}}) \cos^2\bar{\theta} \\ &\quad - (k_t / 2)(\eta l)^2 [2 \cos(2\bar{\theta}) - \beta \cos\bar{\theta}] \delta\theta_0^{\text{inh}}, \end{aligned} \quad (\text{B.1a})$$

$$\begin{aligned} 0 &= k_\theta(\delta\theta_{n+1}^{\text{inh}} + \delta\theta_{n-1}^{\text{inh}} + 4\delta\theta_n^{\text{inh}}) - k_s l^2 (\delta\theta_{n+1}^{\text{inh}} + \delta\theta_{n-1}^{\text{inh}} - 2\delta\theta_n^{\text{inh}}) \cos^2\bar{\theta} \\ &\quad - k_t(\eta l)^2 [2 \cos(2\bar{\theta}) - \beta \cos\bar{\theta}] \delta\theta_n^{\text{inh}}, \quad n \in [1, N-1] \end{aligned} \quad (\text{B.1b})$$

$$\begin{aligned} (Fl \cos\bar{\theta}) / 2 &= k_\theta(\delta\theta_{N-1}^{\text{inh}} + 2\delta\theta_N^{\text{inh}}) - k_s l^2 (\delta\theta_{N-1}^{\text{inh}} - \delta\theta_N^{\text{inh}}) \cos^2\bar{\theta} \\ &\quad - (k_t / 2)(\eta l)^2 [2 \cos(2\bar{\theta}) - \beta \cos\bar{\theta}] \delta\theta_N^{\text{inh}}, \end{aligned} \quad (\text{B.1c})$$

in Eqs. (B.1), the definition of $\delta\theta_n^{\text{inh}}$ is $\delta\theta_n^{\text{inh}} = \delta\theta^{\text{inh}}(X) |_{X=n}$. Since $n \in [1, N-1]$, Eqs. (B.1) corresponds to N' equations. Summing these N' equations, the left term of the summation equation is $Fl \cos\bar{\theta}$. The right term of the summation equation is classified and discussed. For terms with coefficients k_θ ,

$$\begin{aligned} &\delta\theta_1^{\text{inh}} + 2\delta\theta_0^{\text{inh}} + \sum_{n=1}^{N-1} (\delta\theta_{n+1}^{\text{inh}} + \delta\theta_{n-1}^{\text{inh}} + 4\delta\theta_n^{\text{inh}}) + \delta\theta_{N-1}^{\text{inh}} + 2\delta\theta_N^{\text{inh}} \\ &= \sum_{n=1}^{N-1} (\delta\theta_{n-1}^{\text{inh}}) + \delta\theta_{N-1}^{\text{inh}} + \delta\theta_1^{\text{inh}} + \sum_{n=1}^{N-1} (\delta\theta_{n+1}^{\text{inh}}) + 2\delta\theta_0^{\text{inh}} + 4 \sum_{n=1}^{N-1} (\delta\theta_n^{\text{inh}}) + 2\delta\theta_N^{\text{inh}} \\ &= \sum_{n=1}^{N-1} (\delta\theta_n^{\text{inh}} + \delta\theta_{n+1}^{\text{inh}}) + 2 \sum_{n=1}^{N-1} (\delta\theta_n^{\text{inh}} + \delta\theta_{n+1}^{\text{inh}}) \\ &= 3 \sum_{n=1}^{N-1} (\delta\theta_n^{\text{inh}} + \delta\theta_{n+1}^{\text{inh}}). \end{aligned} \quad (\text{B.2})$$

For terms with coefficients k_s ,

$$\begin{aligned}
& \delta\theta_1^{\text{inh}} - \delta\theta_0^{\text{inh}} + \sum_{n=1}^{N-1} (\delta\theta_{n+1}^{\text{inh}} + \delta\theta_{n-1}^{\text{inh}} - 2\delta\theta_n^{\text{inh}}) + \delta\theta_{N-1}^{\text{inh}} - \delta\theta_N^{\text{inh}} \\
&= \delta\theta_1^{\text{inh}} - \delta\theta_0^{\text{inh}} + \sum_{n=1}^{N-1} [(\delta\theta_{n+1}^{\text{inh}} - \delta\theta_n^{\text{inh}}) - (\delta\theta_n^{\text{inh}} - \delta\theta_{n-1}^{\text{inh}})] - (\delta\theta_N^{\text{inh}} - \delta\theta_{N-1}^{\text{inh}}) \\
&= 0.
\end{aligned} \tag{B.3}$$

For terms with coefficients k_t ,

$$\frac{1}{2}\delta\theta_0^{\text{inh}} + \sum_{n=1}^{N-1} (\delta\theta_n^{\text{inh}}) + \frac{1}{2}\delta\theta_N^{\text{inh}} = \frac{1}{2} \sum_0^{N-1} (\delta\theta_n^{\text{inh}} + \delta\theta_{n+1}^{\text{inh}}). \tag{B.4}$$

Combining Eqs. (B.2), (B.3) and (B.4), the summation equation is

$$Fl \cos \bar{\theta} = \left\{ 3k_\theta - \frac{k_t(\eta l)^2}{2} [2 \cos(2\bar{\theta}) - \beta \cos \bar{\theta}] \right\} \sum_0^{N-1} (\delta\theta_n^{\text{inh}} + \delta\theta_{n+1}^{\text{inh}}), \tag{B.5}$$

$\sum_0^{N-1} (\delta\theta_n^{\text{inh}} + \delta\theta_{n+1}^{\text{inh}})$ is expressed as

$$\sum_0^{N-1} (\delta\theta_n^{\text{inh}} + \delta\theta_{n+1}^{\text{inh}}) = \frac{2Fl \cos \bar{\theta}}{6k_\theta - k_t(\eta l)^2 [2 \cos(2\bar{\theta}) - \beta \cos \bar{\theta}]}. \tag{B.6}$$

Substituting Eq. (B.6) into $\Delta L_0 = (\eta l \sin \bar{\theta}) \sum_0^{N-1} (\delta\theta_n^{\text{inh}} + \delta\theta_{n+1}^{\text{inh}})$,

$$\Delta L_0 = \frac{F\eta l^2 \sin(2\bar{\theta})}{6k_\theta - k_t(\eta l)^2 [2 \cos(2\bar{\theta}) - \beta \cos \bar{\theta}]}. \tag{B.7}$$

Combining Eq. (B.7) and the expression of C_θ (Eq. (10)), ΔL_0 can be expressed simply as $2lC_\theta \cos \bar{\theta}$.

(i)-2 Solution for η_e

Substituting the angle solution Eq. (9) and the displacement solution Eq. (12) into Eq. (A.9),

$$\Delta L_e = u_0^{\text{inh}} - u_N^{\text{inh}} + u_0^{\text{h}} - u_N^{\text{h}} + l (\delta\theta_0^{\text{inh}} + \delta\theta_N^{\text{inh}} + 2C_\theta) \cos \bar{\theta}, \tag{B.8}$$

where, $u_n^{\text{inh}} = u^{\text{inh}}(X) |_{X=n}$, $u_n^{\text{h}} = u^{\text{h}}(X) |_{X=n}$ and $\delta\theta_n^{\text{inh}} = \delta\theta^{\text{inh}}(X) |_{X=n}$. In Eq.

(B.8), $u_0^{\text{inh}} - u_N^{\text{inh}} = \Delta L_0$, $u_0^{\text{h}} - u_N^{\text{h}} = D_1 N$ and $\delta\theta_0^{\text{inh}} = \delta\theta_N^{\text{inh}}$, thus, ΔL_e can be

further expressed as

$$\Delta L_e = 2\Delta L_0 + 2l\delta\theta_0^{\text{inh}} + D_1 N. \tag{B.9}$$

According to the expression $\eta_e = \Delta L_e / F$ for compliance,

$$\eta_e(\bar{\theta}, N') = \frac{1}{F} [2\Delta L_0(\bar{\theta}) + 2l\delta\theta_0^{\text{inh}}(\bar{\theta}, N') + D_1(\bar{\theta})N]. \quad (\text{B.10})$$

By Eq. (B.7), $\Delta L_0(\bar{\theta})$ has the symmetry $\Delta L_0(\bar{\theta}) = -\Delta L_0(-\bar{\theta})$. For $\delta\theta_0^{\text{inh}}(\bar{\theta}, N')$,

$$\delta\theta_0^{\text{inh}}(\bar{\theta}, N') = \frac{Fl \cos \bar{\theta} (1 + e^{N/\lambda^*})}{K_1(1 + e^{N/\lambda^*}) - K_2[e^{1/\lambda^*} + e^{(N-1)/\lambda^*}]}, \quad (\text{B.11})$$

since $\lambda^*(\bar{\theta}) = \lambda^*(-\bar{\theta})$, $K_1(\bar{\theta}) = K_1(-\bar{\theta})$ and $K_2(\bar{\theta}) = K_2(-\bar{\theta})$, $\delta\theta_0^{\text{inh}}(\bar{\theta})$ has the symmetry $\delta\theta_0^{\text{inh}}(\bar{\theta}) = \delta\theta_0^{\text{inh}}(-\bar{\theta})$. For $D_1(\bar{\theta})$,

$$D_1(\bar{\theta}) = \frac{2F(\eta_l \sin \bar{\theta})^2}{6k_\theta - k_t(\eta_l)^2(2 \cos(2\bar{\theta}) - \beta \cos \bar{\theta})} + \frac{F}{2k_l}, \quad (\text{B.12})$$

$D_1(\bar{\theta})$ has the symmetry $D_1(\bar{\theta}) = D_1(-\bar{\theta})$.

(i)-3 Monotonicity of $\delta\theta_0^{\text{inh}}(N')$

According to Eq. (17), $\delta\theta_0^{\text{inh}}$ can also be represented by

$$\delta\theta_0^{\text{inh}} = \frac{Fl \cos \bar{\theta}}{K_1 - K_2 \left[\frac{e^{1/\lambda^*} + e^{(N-1)/\lambda^*}}{1 + e^{N/\lambda^*}} \right]}, \quad (\text{B.13})$$

$\delta\theta_0^{\text{inh}}$ is always positive because $\delta\theta_0^{\text{inh}}$ is the response under the positive moment $(Fl \cos \bar{\theta}) / 2$. In the expression for $\delta\theta_0^{\text{inh}}(N')$, the denominator is a positive constant independent of the size, which means that the monotonicity of the function $\delta\theta_0^{\text{inh}}(N')$ can be determined by the monotonicity of the denominator. A function $\varphi(N)$ is defined as

$$\varphi(N) = \frac{e^{1/\lambda^*} + e^{(N-1)/\lambda^*}}{1 + e^{N/\lambda^*}}. \quad (\text{B.14})$$

In Eq. (B.13), $K_2 = 2(k_s l^2 \cos^2 \bar{\theta} - k_\theta) > 0$ is naturally satisfied in a low-torsion shim, so $(d\delta\theta_0^{\text{inh}} / dN')(d\varphi / dN') > 0$, namely, the monotonicity of $\delta\theta_0^{\text{inh}}(N')$ and $\varphi(N)$ is consistent. $\varphi(N)$ is further expressed as

$$\varphi(N) = \frac{e^{1/\lambda^*} + e^{(N-1)/\lambda^*} + e^{-1/\lambda^*} - e^{-1/\lambda^*}}{1 + e^{N/\lambda^*}} = \frac{e^{1/\lambda^*} - e^{-1/\lambda^*}}{1 + e^{N/\lambda^*}} + e^{-1/\lambda^*}. \quad (\text{B.15})$$

$\varphi(N)$ is monotonically decreasing to get $\delta\theta_0^{\text{inh}}(N')$ is also monotonically decreasing, so $\delta\theta_0^{\text{inh}}(N')$ reaches its maximum at the smallest even nodes $N' = 2$.

According to $\Delta L_e^{\text{inh}} = 2l(C_\theta + \delta\theta_0^{\text{inh}}) \cos \bar{\theta}$, the monotonically decreasing $\delta\theta_0^{\text{inh}}(N')$ reveals a characteristic to inhomogeneous deformation, namely, under the same force, the chain with a smaller size has a larger end-to-end displacement. This property is contrary to homogeneous deformation, and it is also contrary to the common perception that increasing size will soften the structure (Yang & Müller, 2021). This characteristic is the fundamental reason for the increase of stiffness with size at small sizes, and this characteristic is closely related to the decay property ($\lambda^* > 0$) of low-energy deformation, since $\lambda^* > 0$ determines the monotonicity of $\varphi(N)$ (or $\delta\theta_0^{\text{inh}}$).

The distribution of inhomogeneous deformation is

$$\delta\theta^{\text{inh}}(X) = C_1 [e^{X/\lambda^*} + e^{(N-X)/\lambda^*}]. \quad (\text{B.16})$$

When the size is large enough, the low-energy deformation modes at both ends are localized on their respective sides. Taking the left deformation $\delta\theta^{\text{inh}}(0) = C_1 + C_1 e^{N/\lambda^*}$ as an example, the deformation $C_1 e^{N/\lambda^*}$ can be seen as the deformation of the left low-energy mode at $X=0$, and deformation C_1 is the superposition of the right low-energy deformation to the left low-energy deformation at $X=0$. For a long enough chain, $C_1 \ll C_1 e^{N/\lambda^*}$, namely, the low-energy deformations at both ends almost do not produce superposition, and the deformation near the left end can be expressed as

$$\delta\theta^{\text{inh}}(X) = C_1 e^{(N-X)/\lambda^*}. \quad (\text{B.17})$$

Substituting Eq. (B.17) into Eq. (B.1a),

$$\delta\theta_0^{\text{inh}} = \frac{Fl \cos \bar{\theta}}{K_1 - K_2 e^{-1/\lambda^*}}, \quad (\text{B.18})$$

denoting the right term of Eq. (B.18) as $\delta\theta_0^{\text{inh}*}$, $\delta\theta_0^{\text{inh}*}$ is the characteristic deformation of the 0-th node in the semi-infinite chain. Since $\delta\theta_0^{\text{inh}}(N')$ is monotonically decreasing and has a lower bound 0, $\delta\theta_0^{\text{inh}*}$ is the limit of $\delta\theta_0^{\text{inh}}(N')$,

$$\lim_{N' \rightarrow \infty} \delta\theta_0^{\text{inh}}(N') = \delta\theta_0^{\text{inh}*}. \quad (\text{B.19})$$

Eq. (B.19) shows that as the size increases, $\delta\theta_0^{\text{inh}}(N')$ converges to a size-independent characteristic quantity $\delta\theta_0^{\text{inh}*}$, which means inhomogeneous

deformation can only lead to an increase in stiffness, the decreasing behavior of stiffness after the size reaches $N_{P'}$ is completely caused by homogeneous deformation. For the convergence of $\delta\theta_0^{\text{inh}}(N')$ to $\delta\theta_0^{\text{inh}*}$, another qualitative conclusion can be given: If $\delta\theta^{\text{inh}}(X)$ decays quickly, then the superposition effect of deformation has disappeared at short nodes, and $\delta\theta_0^{\text{inh}}(N')$ will rapidly converge to $\delta\theta_0^{\text{inh}*}$, which means that $N_{P'}$ is small. In other words, a larger $N_{P'}$ must correspond to a slower decay rate, and this conclusion is used in the analysis of the relative error in Section 4.2.

Meanwhile, Eq. (B.19) also reveals the underlying logic that λ^* can be used as the characteristic quantity of the anomalous size effects. In the process of size increase, the convergence of $\delta\theta_0^{\text{inh}}(N')$ to $\delta\theta_0^{\text{inh}*}$ actually corresponds to the convergence of the decay length λ of the finite structure to the characteristic decay length λ^* , because both of these convergence can be equivalent to the approximation of Eq. (B.16) to Eq. (B.17). Therefore, we can estimate stiffness monotonicity based on the difference between λ and λ^* , but we cannot uniformly give the critical point at which stiffness monotonicity transitions by making $\lambda - \lambda^*$ equal to a specific value.

(ii) Continuum model for odd nodes

In (ii) section, the modeling details of the continuum model for odd nodes in Fig. 2(b) are shown.

For a chain with odd nodes, although the load is symmetric, this structure is not axisymmetric. Therefore, the axisymmetry cannot be used to simplify the model, and the form of the solution is set to

$$\delta\theta = C_1 e^{X/\lambda^*} + C_2 e^{(N-X)/\lambda^*} + C_\theta. \quad (\text{B.20})$$

Eq. (B.20) is substituted into Eq. (6), the displacement solution for the odd-node chain is obtained,

$$u = -2\eta l \lambda^* [C_1 e^{X/\lambda^*} - C_2 e^{(N-X)/\lambda^*}] \sin \bar{\theta} - D_1 X + D_2. \quad (\text{B.21})$$

There are 5 integral constants, where D_2 is the rigid body translation mode it does not need to be determined, the integral constants C_θ and D_1 corresponding to

homogeneous deformation are determined directly by physical sense (namely, Eq.(10) and Eq.(15)), the integral constants C_1 and C_2 corresponding to the inhomogeneous deformation are determined by the boundary conditions Eqs. (3a) and (3c), namely,

$$\begin{bmatrix} a_{11} & a_{12} \\ a_{21} & a_{22} \end{bmatrix} \begin{bmatrix} C_1 \\ C_2 \end{bmatrix} = \frac{1}{2} \begin{bmatrix} Fl \cos \bar{\theta} \\ -Fl \cos \bar{\theta} \end{bmatrix}. \quad (\text{B. 22})$$

Let $\alpha(\bar{\theta})=2 \cos(2\bar{\theta}) - \beta \cos \bar{\theta}$, the coefficient matrix in the Eq. (B.22) is

$$\begin{bmatrix} a_{11} \\ a_{12} \\ a_{21} \\ a_{22} \end{bmatrix} = \begin{bmatrix} e^{1/\lambda^*} + 2 & e^{1/\lambda^*} - 1 & 1 \\ e^{-1/\lambda^*} + 2 & e^{-1/\lambda^*} - 1 & 1 \\ e^{(N-1)/\lambda^*} + 2e^{N/\lambda^*} & e^{(N-1)/\lambda^*} - e^{N/\lambda^*} & e^{N/\lambda^*} \\ e^{-(N-1)/\lambda^*} + 2e^{-N/\lambda^*} & e^{-(N-1)/\lambda^*} - e^{-N/\lambda^*} & e^{-N/\lambda^*} \end{bmatrix} \begin{bmatrix} k_\theta \\ -k_s t^2 \\ -\frac{k_t(\eta l)^2}{2} \alpha(\bar{\theta}) \end{bmatrix}.$$

References

- Deng, B., Raney, J. R., Bertoldi, K., Tournat, V., 2021. Nonlinear waves in flexible mechanical metamaterials. *Journal of Applied Physics*, 130 (4), 040901.
- Bertoldi, K., Reis, P. M., Willshaw, S., Mullin, T., 2010. Negative Poisson's Ratio Behavior Induced by an Elastic Instability. *Advanced Materials*, 22 (3), 361-366.
- Dudek, K. K., Iglesias Martínez, J. A., Ulliac, G., Hirsinger, L., Wang, L., Laude, V., Kadic, M., 2023. Micro-Scale Mechanical Metamaterial with a Controllable Transition in the Poisson's Ratio and Band Gap Formation. *Advanced Materials*, 35 (20), 2210993.
- Khan, K. A., Alshaer, M. H., Khan, M. A., 2021. A Novel Twofold Symmetry Architected Metamaterials with High Compressibility and Negative Poisson's Ratio. *Advanced Engineering Materials*, 23 (5), 2001041.
- Deng, B., Raney, J. R., Tournat, V., Bertoldi, K., 2017. Elastic Vector Solitons in Soft Architected Materials. *Physical Review Letters*, 118 (20), 204102.
- Li, J., Yuan, Y., Wang, J., Bao, R., Chen, W., 2021. Propagation of nonlinear waves in graded flexible metamaterials. *International Journal of Impact Engineering*, 156, 103924.
- Zhang, Q., Cherkasov, A. V., Xie, C., Arora, N., Rudykh, S., 2023. Nonlinear elastic vector solitons in hard-magnetic soft mechanical metamaterials. *International Journal of Solids and Structures*, 280, 112396.
- Liu, W., Janbaz, S., Dykstra, D., Ennis, B., Coulais, C., 2024. Harnessing plasticity in sequential metamaterials for ideal shock absorption. *Nature*, 634 (8035), 842-847.
- Demiquel, A., Achilleos, V., Theocharis, G., Tournat, V., 2024. Envelope vector solitons in nonlinear flexible mechanical metamaterials. *Wave Motion*, 131, 103394.
- Liang, X., Crosby, A. J., 2020. Programming Impulsive Deformation with Mechanical Metamaterials. *Physical Review Letters*, 125 (10), 108002.
- Jiao, W., Shu, H., Tournat, V., Yasuda, H., Raney, J. R., 2024. Phase transitions in 2D multistable mechanical metamaterials via collisions of soliton-like pulses. *Nature Communications*, 15 (1), 333.
- Meeussen, A. S., Bordiga, G., Chang, A. X., Spoettling, B., Becker, K. P., Mahadevan, L., Bertoldi, K., 2024. Textile Hinges Enable Extreme Properties of Kirigami Metamaterials. *Advanced Functional Materials*, 2415986.
- Mizzi, L., Spaggiari, A., 2020. Lightweight mechanical metamaterials designed using hierarchical truss elements. *Smart Materials and Structures*, 29 (10), 105036.
- Zhou, Y., Zhang, Y., Chen, C. Q., 2021. Amplitude-dependent boundary modes in topological mechanical lattices. *Journal of the Mechanics and Physics of Solids*, 153, 104482.
- Ma, J., Zhou, D., Sun, K., Mao, X., Gonella, S., 2018. Edge Modes and Asymmetric Wave Transport in Topological Lattices: Experimental Characterization at Finite Frequencies. *Physical Review Letters*, 121 (9), 094301.
- Kane, C. L., Lubensky, T. C., 2014. Topological boundary modes in isostatic lattices. *Nature Physics*, 10 (1), 39-45.
- Coulais, C., Sounas, D., Alù, A., 2017. Static non-reciprocity in mechanical metamaterials. *Nature*, 542 (7642), 461-464.
- Chen, B. G.-g., Upadhyaya, N., Vitelli, V., 2014. Nonlinear conduction via solitons in a topological mechanical insulator. *Proceedings of the National Academy of Sciences*, 111 (36), 13004-13009.

- Ma, F., Tang, Z., Shi, X., Wu, Y., Yang, J., Zhou, D., et al., 2023. Nonlinear Topological Mechanics in Elliptically Geared Isostatic Metamaterials. *Physical Review Letters*, 131 (4), 046101.
- Demiquel, A., Achilleos, V., Theocharis, G., Tournat, V., 2023. Modulation instability in nonlinear flexible mechanical metamaterials. *Physical Review E*, 107 (5), 054212.
- Li, Y., Yan, S., Li, H., 2022. Wave propagation of 2D elastic metamaterial with rotating squares and hinges. *International Journal of Mechanical Sciences*, 217, 107037.
- Vahabi, M., Sharma, A., Licup, A. J., van Oosten, A. S. G., Galie, P. A., Janmey, P. A., MacKintosh, F. C., 2016. Elasticity of fibrous networks under uniaxial prestress. *Soft Matter*, 12 (22), 5050-5060.
- Tang, Z., Ma, T., Chen, H., Gao, Y., 2024. Evolution of static to dynamic mechanical behavior in topological nonreciprocal active metamaterials. *Journal of the Mechanics and Physics of Solids*, 193, 105865.
- Deng, B., Yu, S., Forte, A. E., Tournat, V., Bertoldi, K., 2020. Characterization, stability, and application of domain walls in flexible mechanical metamaterials. *Proceedings of the National Academy of Sciences*, 117 (49), 31002-31009.
- Czajkowski, M., Coulais, C., van Hecke, M., Rocklin, D. Z., 2022. Conformal elasticity of mechanism-based metamaterials. *Nature Communications*, 13 (1), 211.
- Medina, E., Rycroft, C. H., Bertoldi, K., 2023. Nonlinear shape optimization of flexible mechanical metamaterials. *Extreme Mechanics Letters*, 61, 102015.
- Zhang, Y., Li, B., Zheng, Q. S., Genin, G. M., Chen, C. Q., 2019. Programmable and robust static topological solitons in mechanical metamaterials. *Nature Communications*, 10 (1), 5605.
- Florijn, B., Coulais, C., van Hecke, M., 2014. Programmable Mechanical Metamaterials. *Physical Review Letters*, 113 (17), 175503.
- Zheng, Y., Niloy, I., Celli, P., Tobasco, I., Plucinsky, P., 2022. Continuum Field Theory for the Deformations of Planar Kirigami. *Physical Review Letters*, 128 (20), 208003.
- Liang, X., Crosby, A. J., 2020. Uniaxial stretching mechanics of cellular flexible metamaterials. *Extreme Mechanics Letters*, 35, 100637.
- Li, J., Bao, R., Chen, W., 2024. Exploring static responses, mode transitions, and feasible tunability of Kagome-based flexible mechanical metamaterials. *Journal of the Mechanics and Physics of Solids*, 186, 105599.
- Kadic, M., Frenzel, T., Wegener, M., 2018. When size matters. *Nature Physics*, 14 (1), 8-9.
- Ziemke, P., Frenzel, T., Wegener, M., Gumbsch, P., 2019. Tailoring the characteristic length scale of 3D chiral mechanical metamaterials. *Extreme Mechanics Letters*, 32, 100553.
- Coulais, C., Kettenis, C., van Hecke, M., 2018. A characteristic length scale causes anomalous size effects and boundary programmability in mechanical metamaterials. *Nature Physics*, 14 (1), 40-44.
- Frenzel, T., Kadic, M., Wegener, M., 2017. Three-dimensional mechanical metamaterials with a twist. *Science*, 358 (6366), 1072-1074.
- Tang, Z., Ma, T., Li, S., Chen, H., Su, B., Kang, P., et al., 2023. Polarization-dependent boundary modes in nonlinear mechanical metamaterials. *International Journal of Mechanical Sciences*, 258, 108584.
- Schiøtz, J., Di Tolla, F. D., Jacobsen, K. W., 1998. Softening of nanocrystalline metals at very small grain sizes. *Nature*, 391 (6667), 561-563.
- Peng, H. R., Jian, Z. Y., Liu, C. X., Huang, L. K., Ren, Y. M., Liu, F., 2022. Uncovering the softening

- mechanism and exploring the strengthening strategies in extremely fine nanograined metals: A molecular dynamics study. *Journal of Materials Science & Technology*, 109, 186-196.
- Wheel, M. A., Frame, J. C., Riches, P. E., 2015. Is smaller always stiffer? On size effects in supposedly generalised continua. *International Journal of Solids and Structures*, 67-68, 84-92.
- Yang, H., Müller, W. H., 2021. Size effects of mechanical metamaterials: a computational study based on a second-order asymptotic homogenization method. *Archive of Applied Mechanics*, 91 (3), 1037-1053.